scientific reports

Check for updates

OPEN

Lung cancer exosomal Gal3BP promotes osteoclastogenesis with potential connotation in osteolytic metastasis

Pratyusha Ghanta[1,2], Evin Hessel[1], Andrea Arias-Alvarado[1], Mirjavid Aghayev[1], Serguei Ilchenko[1], Takhar Kasumov[1] & Moses O. Oyewumi[1,3 ✉]

New insights into cellular interactions and key biomolecules involved in lung cancer (LC) bone metastasis could offer remarkable therapeutic benefits. Using a panel of four LC cells, we investigated LC-bone interaction by exposing differentiating osteoclasts (OCs) to LC cells (LC-OC interaction) directly in a co-culture setting or indirectly via treatment with LC secretomes (conditioned media or exosomes). LC-OC interaction facilitated the production of large-sized OCs (nuclei > 10) coupled with extensive bone resorption pits. Proteomic analysis of LC exosomes identified galectin-3-binding protein (Gal3bp) as a potential biomarker which was released primarily by most of LC-derived exosomes. The facilitation of OC differentiation and function by LC-exosomal Gal3bp was supported by the application of recombinant Gal3bp and anti-Gal3bp in OC treatment. Further, our results exhibited a dysregulation of crucial OC markers (TRAF6, p-SAPK/JNK, p-44/42 MAPK, NFAT2 and CD9) during LC-OC interaction that possibly contributed to the facilitation of osteoclastogenesis. Simulation of bone metastasis via intratibial injection of LC cells revealed Gal3bp's possible roles in enhancing OC activation leading to osseous tissue resorption. Overall, this work implicated LC-exosomal Gal3bp in osteolytic metastasis of LC which warrants further studies to assess its potential prognostic and therapeutic relevance.

Lung cancer (LC) ranks among the foremost causes of cancer-related fatalities and its mortality rate continues to rise with a 5-year survival rate of less than 10% [1,2]. The ominous prognosis is largely due to its propensity to metastasize as the disease progresses. This entails the infiltration of multiple sites, including but not limited to the brain, liver, kidneys, and skeletal system[3]. A shared characteristic of these metastatic sites is the availability of a nurturing environment for the proliferation and colonization of metastatic LC cells[4]. The bone, composed of a rich cell population within the stroma, matrix, and fenestrated capillaries, presents an attractive environment for metastasizing LC cells[1,5,6]. The invasion of LC cells into the osseous tissue occurs through a metastasis cascade in which LC cells undergo epithelial-mesenchymal transition (EMT), involving multiple processes such as E-cadherin suppression via Wnt signaling[7] and upregulation of pathways involving epithelial growth factors (EGFs) or EGF like domains[8]. Upon completion of the transition process, metastatic cells are able to gain access to the circulatory or lymphatic systems and migrate to secondary areas, such as bone tissue[1].

Bone metastasis (BM) can be classified into osteolytic (excessive bone resorption), osteoblastic (abnormal bone formation), or mixed (combination of both excessive bone resorption and growth) based on the type of cancer invading into the bone[9]. In LC, BM (occurring in 40% of patients[10,11]) is associated with an osteolytic effect resulting in excessive osteoclast (OC) activity characterized by osteolytic lesions[12]. These lesions can often result in skeletal issues such as pain, hypercalcemia, spinal cord compression and pathological fractures and may impede effectiveness of treatment strategies[6,13]. The process of BM involves the release of active biomolecules by LC cells for effective integration into the host environment feeding into the "seed and soil" phenomena[14,15]. These biomolecules, known as tumor-secreted factors or secretomes, have been extensively studied to elucidate the underlining mechanisms of the BM process[16]. For example, formin-like protein 1 (FMNL1) was found to

[1]Department of Pharmaceutical Sciences, College of Pharmacy, Northeast Ohio Medical University, Rootstown, OH 44272, USA. [2]Department of Biomedical Sciences, Kent State University, Kent, OH 44240, USA. [3]Department of Pharmaceutical Sciences, UH-NEOMED Faculty Scholar, Northeast Ohio Medical University, 4209 State Route 44, Rootstown, OH 2024, 44272, USA. ✉email: moyewumi@neomed.edu

be upregulated in LC metastasized bone tissue through the TGF-β1/SMAD signaling pathway, which enhanced EMT and promoted BM[17]. Similarly, another study showed that fas apoptotic inhibitor molecule 2 (FAIM2) was significantly upregulated in LC tissues and activated the EMT process via the Wnt/β-catenin signaling pathway[18].

Extracellular vesicles (EVs) such as exosomes that are released by LC cells have been implicated in cellular communication and BM signaling pathways[19–21]. Exosomes are lipid-coated vesicles (diameter of 30–150 nm[22,23]) that envelope various active biomolecules such as nucleic acids, proteins, lipids, enzymes, and metabolites[24]. It has been strongly suggested that LC-derived exosomes (LC-Exo) facilitated cancer progression and invasion to the bone. For instance, LC-exosomal miR-328[25] and miR-17-5p[26] have been reported to enhance OC resorption by targeting the PI3K/Akt pathway and downregulating Nrp-2 and PTEN expression, respectively. Similarly, A549 exosomal lncRNA HOTAIR[27] was suggested to promote OC differentiation and bone resorption by targeting miRNA-194-5p and increasing RAC1 expression, leading to overstimulation of the TGF-β/pTHrP/RANKL pathway and suppression of OPG, respectively. LC-exosomal SOX2OT has also been reported to influence osteoclastogenesis via a similar pathway[10].

This study examined the potential role of LC-derived exosomal galectin-3-binding protein (Gal3bp) in OC differentiation and resorption. Gal3bp is a multifunctional hyperglycosylated protein member of the scavenger cysteine-rich domain family of proteins[28]. Based on ligand binding studies, Gal3bp has been reported to undergo glycosylation via proteolytic cleavage, which is commonly observed in neoplastic conditions[29]. Gal3bp's expression was previously reported to facilitate pathological conditions such as lupus[30], COVID[31], cancer (breast[32], pancreatic[33], and colon[34]), venous thrombosis[30], and HIV[35]. The galectin family of proteins have been linked to cancer progression, angiogenesis, and metastasis[36,37]. Meanwhile, the role of Gal3bp in OC differentiation and function has not been fully elucidated, which formed the basis of the work herein.

In the study, we applied a panel of LC cells (A549, H1437, SK MES-1, and Calu-6) to reflect the heterogeneous nature of LC in our findings. We assessed the effects of LC cells on differentiating OCs directly via co-incubation or indirectly via treatment with LC secretomes (conditioned media and exosomes). We paid particular attention to exosomes derived from the panel of LC cells (LC-Exo) and investigated potential proteins that are enveloped within its structure. Using mass spectrometry, we subjected LC-Exo to proteomic analysis to identify novel LC-BM markers that led to the selection to Gal3bp. This work hypothesizes that exosomal secretion of Gal3bp by LC cells facilitates OC differentiation and function which could support osteolytic bone lesions. LC-OC interaction was simulated through co-incubation and treatment of OCs with LC secretomes. Further, using athymic nu/nu mice, we induced BM by intratibial injection of LC cells and assessed the extent of bone destruction alone or in combination with recombinant Gal3bp. The findings from our work suggest that LC exosomal Gal3bp may play a pivotal role in promoting osteoclastogenesis with the possibility of serving as a novel biomarker for LC-BM.

Materials and methods
Cell culture
A panel of non-small cell lung cancer cell lines; A549 (human lung adenocarcinoma), A549-Luc2 (human lung adenocarcinoma expressing firefly luciferase gene), H1437 (stage 1 human NSCLC adenocarcinoma), SK MES-1 (human lung squamous cell carcinoma), and Calu-6 (human anaplastic carcinoma) were procured from ATCC (Manassas, VA). The A549 cell line was maintained in Dulbecco's modified Eagle's medium (DMEM-Corning Inc, Corning, NY), the H1437 cell line was maintained in RPMI-1640 (Corning Inc, Corning, NY), and the SK MES-1 and Calu-6 cell lines were grown in MEM (Corning Inc, Corning, NY). All the above media were supplemented with 10% fetal bovine serum (FBS; Fisher Scientific, Waltham, MA) and 1% penicillin-streptomycin (PenStrep; Gibco, Grand Island, NY). A549-Luc2 was maintained in F-12 K complete media (ATCC, Manassas, VA).

BEAS-2b cells (human lung epithelial) and RAW 264.7 cells (murine macrophage- OC precursor, pre-OC cells) were procured from ATCC. BEAS-2b was maintained in a BEGM media kit (Lonza Bioscience, Walkersville, MD) supplemented with 8 µg/mL blasticidin HCl (Fisher Scientific, Waltham, MA). RAW 264.7 cells were grown in complete DMEM media supplemented with 10% FBS (Fisher Scientific, Waltham, MA) and 1% PenStrep (Gibco, Grand Island, NY). All cells were incubated at 37ºC in 5% CO_2 conditions and, upon 60–70% confluency, the monolayer was washed with 1x PBS (Cytiva Life Science, Marlborough, MA) and gently detached using a cell scraper for RAW 264.7 cells and 0.25% v/v trypsin/EDTA (Cytiva Life Science, Marlborough, MA) for the remaining cell lines. The detached cell suspension was collected, centrifuged at 423xg for 5 min, and seeded according to the requirement for each assay.

Isolation and characterization of LC secretomes
Preparation of conditioned media from LC (LC-CM)
LC cells were cultured in 182 cm^2 flasks to 80% confluence and rinsed twice with 1x PBS prior to incubation with 25 mL of serum-free respective growth media for 24 h. The conditioned media was collected, centrifuged (423xg, 5 min), filtered (0.2 µm filter, CellTreat Scientific Products, Pepperell, MA), and stored (-80 °C) until further analysis[38].

Exosome isolation & characterization from LC cells (LC-Exo)
Exosomes released by LC cells were isolated via differential centrifugation as mentioned previously[39]. Briefly, at 65–70% confluency, the media was aspirated and replenished with growth media supplemented with 10% EV depleted FBS (Gibco, Grand Island, NY) and 1% PenStrep. After 24 h, the media was collected and subjected to consequent centrifugal and ultracentrifugal speeds for exosome isolation, i.e., 300xg for 10 min, 2000xg for 20 min, 10000xg for 40 min, and 110,000xg for 70 min. The obtained pellet was washed and resuspended in PBS, followed by ultracentrifugation at 110,000xg for 70 min. A similar procedure was followed for isolating

exosomes from BEAS-2b (healthy human lung epithelial) cells (BEAS-2b-Exo). The exosomal protein content was determined by the Pierce BCA assay as per the manufacturer's instructions (ThermoFisher Scientific, Waltham, MA). The isolated exosomes were characterized as per previous reports[40] by analyzing and visualizing exosome size using a dynamic light scattering (DLS) Malvern zeta sizer (Malvern Panalytical, Worcestershire, UK) and TEM imaging. To further characterize the isolated exosomes, the presence of exosomal markers CD63, TSG101, and ALIX (Cell Signaling, Danvers, MA) were assessed via 10% SDS-PAGE western blotting[41,42].

Transmission electron microscopy (TEM)

Isolated exosomes were incubated and fixed in 2% paraformaldehyde onto a formvar carbon coated EM grid (Ted Pella Inc, Redding, CA). After which, grids were washed with 1x PBS, followed by 1% glutaraldehyde (Polysciences, Warrington, PA) incubation and washing with distilled water. For contrast stain, the grids containing the exosomes were exposed to uranyless EM stain (Electron Microscopy Sciences, Hatfield, PA), followed by 3% lead citrate (Electron Microscopy Sciences, Hatfield, PA). The grids were rinsed, dried and imaged using a Tecnai G2 F20 TEM (FEI Company, Hillsboro, OR)[40].

MTT Assay on Pre-OCs

The following agents were applied to pre-OCs (RAW 264.7 cells) and incubated for 24 h: rGal3bp (0-100 ng/mL), anti-Gal3bp (0–5 µg/mL), undiluted LC-CM, and 50 µg/mL LC-Exo. Afterwards, the content of each well was aspirated, and the potential effects on pre-OCs was assessed via MTT (Sigma Aldrich, St. Louis, MO) as described previously[43]. Optical density of the wells was analyzed at 570 nm and fold change was calculated based on control (untreated) cells as a reference.

OC differentiation and function studies

Treatment with LC secretomes

The effect of LC cells on the extent of OC differentiation was assessed using treatment with LC secretomes such as conditioned media and exosomes. OCs were differentiated from precursor (RAW 264.7) cells as per a previous report[44]. Briefly, RAW 264.7 cells were seeded at a density of 1.5×10^5 cells/cm^2 (day 0) in a 96-well plate and were treated the next day (day 1) with 200 µL of DMEM supplemented with 30 ng/mL of RANKL alone (positive control- R&D Technologies, Minneapolis, MN) or RANKL (30 ng/mL) together with either undiluted LC-CM, 50 µg/mL of LC-Exo, or varying concentrations of recombinant Gal3bp (rGal3bp, 5–50 ng/mL, Bio-Techne, Minneapolis, MN). After 48 h of incubation (day 3), all wells were aspirated and supplemented with fresh media alone (blank) or supplemented with 30 ng/mL RANKL. Matured OCs were evaluated the next day (day 4) for the extent of OC differentiation based on tartrate-resistant acid phosphatase (TRAP) activity and stain for a quantitative analysis ($n=4$) on the number of multinucleated differentiated OCs (≥ 3 nuclei, pink-colored). Images were also taken using a Nikon Eclipse Ti2 Inverted microscope (Nikon Instruments Inc., Melville, NY) for qualitative purposes to observe the potential difference in the differentiated OCs between groups.

LC-OC co-culture method

Using 24-well transwell plates with 0.4 µm inserts (Corning Inc, Corning, NY), pre-OC cells (RAW 264.7) were cultured on the bottom portion of the plate at a seeding density of 5×10^5 cells/well and LC cells were seeded on the top portion at 5×10^2 cells/well (day 0) in their respective media. The next day (day 1), media was aspirated from both portions, and the top insert was placed within the basal portion as per previous protocols[42]. The top inserts were supplemented with fresh media (complete DMEM) and the bottom wells were replenished with fresh media alone (blank) or supplemented with 30 ng/ml RANKL (day 1 and 3). On day 4, the extent of OC differentiation based on the treatments was quantified via TRAP activity and TRAP-stained multinucleated OC count as stated above. Representative images of the differentiated OCs were imaged using a Nikon Eclipse Ti2 Inverted microscope (Nikon Instruments Inc., Melville, NY).

Ex-vivo bone resorption assay

To assess the effects of LC-secretomes, LC cells, and rGal3bp on OC function, a pit resorption assay was conducted using bovine cortical bone slices (BioVendor R&D*, Asheville, NC) as per previous protocols[44,45]. Concisely, RAW 264.7 cells were seeded at 7.5×10^3 cells/well in complete DMEM on the surface of sanitized bovine cortical bone slices (day 0). To initiate differentiation, the wells were aspirated and replenished the following day (day 1) with fresh DMEM media alone (blank), DMEM supplemented with 30 ng/mL RANKL alone (positive control), or DMEM supplemented with 30 ng/mL RANKL combined with one of the following treatments: 50 µg/mL of LC-derived exosomes, LC cells using a transwell plate, or rGal3bp (12.5, 25 and 50 ng/mL). On day 3, subsequent treatment with complete DMEM media containing 30 ng/mL RANKL was administered to all wells (except for blank wells). On day 4, the bone slices were stained via 0.5% toluidine blue (Sigma Aldrich, St. Louis, MO) and imaged using a Nikon Eclipse Ti2 Inverted microscope (Nikon Instruments Inc; Melville, NY). The representative images were used for obtaining the percentage area of resorption on the bone slice using ImageJ (NIH, Bethesda, MD).

Characterization and identification of proteins in LC-Exo

Proteomic analysis

LC-Exo or BEAS-2b-Exo were lysed and the protein content was extracted and analyzed via mass spectrometry analysis as per previous protocols[46,47]. In brief, the exosomes were lysed via 1x RIPA buffer (EMD Millipore Corp, Billerica, MA), and the protein content was quantified using a Pierce BCA kit (Thermofisher Scientific, Waltham, MA). All samples were diluted to the same concentrations (20 µg) and loaded into a 10% SDS-page

gel (BioRad, Hercules, CA), undergoing gel electrophoresis for 15 min, followed by staining and destaining with 0.1% Coomassie blue (BioRad, Hercules, CA) and a 10% acetic acid/ 40% methanol mixture respectively ($n=3$ per group). The bands were excised at the area which was visibly stained and placed in tubes followed by subsequent washings to remove excess dye. The gel fragments were then reduced with 10 mM DTT (Sigma Aldrich, St Louis, MO), alkylated with 55 mM iodoacetic acid (Sigma Aldrich, St Louis, MO), digested with 10 ng/μL trypsin (Promega, Madison, WI), and extracted using 50% acetonitrile and 5% formic acid (Sigma Aldrich, St Louis, MO). The extracted peptides were purified using C18 columns. Proteomic analysis was performed using Ultimate 3000 UHPLC (Thermo Scientific, CA), coupled online to Q Exactive™ Plus Hybrid Quadrupole-Orbitrap™ Mass Spectrometer (Thermo 214 Scientific, CA) for label-free quantification. For protein/peptide identification, all the MS/MS spectra were transformed into a Mascot Generic Format (MGF) peak list file and searched using the Mascot 2.3 (Matrix Science, London, UK) software against the UniProt human protein database released in 2024_02 (03/27/2024, 248,805,733 entries). Protein expressions were assessed by quantifying tryptic peptides using MaxQuant Software (V1.5.2.8). Additional gene ontology analysis was conducted using DavidGO (v2024q2; https://david.ncifcrf.gov/)[48]. For label-free quantification, the MaxLFQ algorithm measured the area under the curve of high-intensity paired peptide signals from the samples in each group ($n=3$) while the results were normalized relative to controls.

Protein analysis using automated Western blot system (ProteinSimple JESS)
Protein expressions of Gal3bp and Gal3 in LC cells or LC-Exo were measured using the capillary-based ProteinSimple JESS system (ProteinSimple, San Jose, CA). Samples from BEAS-2b cells were used as reference control. Respective cells and exosome samples were lysed with 1x RIPA buffer (EMD Millipore Corp, Billerica, MA) supplemented with 1x protease inhibitor cocktail (Thermofisher, Scientific, Waltham, MA), followed by protein quantification using a Pierce BCA protein assay kit (Thermofisher Scientific). Briefly, 0.4 mg/mL of LC-Exo or cell lysates were prepared after dilution with sample buffer and mixed with the manufacturer's master-mix (1x fluorescent standard, 1x sample buffer, and 40 mM dithiothreitol; ProteinSimple, San Jose, CA). The sample mixtures were denatured at 95 °C for 5 min and spun down. The following were added to the appropriate assay plate (12–230 kDa); samples, biotinylated ladder, primary antibodies (anti-Gal3bp and anti-Gal3- 0.2 μg/mL, Bio-Techne, Minneapolis, MN/ ProteinSimple, San Jose, CA) and HRP-conjugated anti-goat secondary antibody (1:1000; Cell Signaling Technology, Danvers, MA) diluted in a milk-free buffer, RePlex™ reagent mix for protein normalization, and luminol/peroxide mix as a chemiluminescent substrate (Bio-Techne, Minneapolis, MN/ProteinSimple, San Jose, CA). The chemiluminescent reactions were analyzed by the Compass software (ProteinSimple, San Jose, CA) using total protein as a loading control[49].

Gal3bp measurement by ELISA
Gal3bp ELISA (Abcam, Cambridge, United Kingdom) was used to quantify the expression of Gal3bp in LC-Exo and BEAS-2b-Exo, cell lysates and LC-CM following the manufacturer's protocol. Briefly, samples were incubated in triplicate for 90 min, followed by incubation with the biotinylated antibody for 1 h. After washing, wells were incubated with ABC working solution, washed again, and incubated with TMB Color Developing Agent, followed by stop solution prior to measurement at 450 nm using a SpectraMax M5 Plate Reader (Molecular Devices, San Jose, CA). Average optical density values were recorded and compared to a standard curve to determine the concentration.

Traditional Western blot analysis
Differentiating OCs co-incubated with LC cells were subjected to western blot analysis on day 4 to assess changes in the expression levels of OC differentiation markers as per the previous protocol[27]. Briefly, the cells were lysed with 1x RIPA lysis buffer (EMD Millipore Corp, Billerica, MA) supplemented with 1x protease inhibitor cocktail (Thermofisher Scientific, Waltham, MA) and quantified for their protein content via a Pierce BCA protein assay kit (Thermofisher Scientific, Waltham, MA). Protein samples (20 μg) were separated via TGX criterion or 10% SDS page gels (Bio-Rad, Hercules, CA) and transferred onto a TransBlot * Turbo™ Mini size polyvinylidene fluoride (PVDF) membrane (Bio-Rad, Hercules, CA). The membrane was blocked with 5% BSA (Fisher Scientific, Pittsburgh, PA), washed (1xTBST) and probed with the following antibodies overnight at 4 °C: anti-p42/44 MAPK (42, 44 kDa, 1:1000), anti- p-SAPK/JNK (46, 54 kDa, 1:1000), anti-CD9 (22, 24, 35 kDa, 1:1000), anti-NFAT2 (140 kDa, 1:1000), anti-CD40/TRAP (31 kDa, 1:1000) (Abcam, Cambridge, United Kingdom) anti-TRAF6 (60 kDa 1:1000), anti-cFos (62 kDa, 1:1000) and DC-Stamp (100 kDa, 1:500, Novus Biologics, Centennial, CO). The blots were probed with a respective HRP conjugated anti-rabbit secondary antibody (1:1000) and visualized via the Fluorchem system (ProteinSimple, San Jose, CA). The immunoblots were further quantified using densitometry analysis via ImageJ and normalized with loading control (GAPDH) bands. All antibodies not otherwise stated were purchased from Cell Signaling Technology (Danvers, MA).

Intratibial injection of LC cells in athymic mice (nu/nu)
All animals were handled according to the protocol approved by the Institutional Animal Care and Use Committee (IACUC) at Northeast Ohio Medical University, IACUC protocol 23-05-369. Athymic mice (nu/nu) were purchased from Charles River Laboratories (Wilmington, MA). We confirm that all experiments were performed in accordance with ARRIVE guidelines. Briefly, the athymic mice (nu/nu, female 8 weeks, $n=3/4$ per group) were administered with 1 mg/kg of buprenorphine SR subcutaneously, and anesthetized with 2% inhalational isoflurane, followed by intratibial administration of A549-Luc2 cells (2.5×10^5 cells) into the left tibia[2,38,50]. The following agents were injected into the tibia according to animal groupings: 25 ng/mL rGal3bp alone, A549-Luc2 alone, or A549-Luc2 supplemented with rGal3bp. Anesthetized mice were injected by exposing the proximal end of the left tibia via flexion and respective agents suspended in PBS were injected into the bone

marrow space. Intratibial tumor growth was monitored for 30 days through weekly bioluminescence imaging using IVIS Lumina XRMS series III (PerkinElmer, Shelton, CT). Before imaging, each mouse was injected with D-Luciferin potassium salt (100 mg/kg, GoldBio, St. Louis, MO) intraperitoneally as mentioned in previous reports[51]. The mice were anesthetized with 2% inhalational isoflurane and imaged under bioluminescent settings using automatic exposure and an open emission filter. Bioluminescence imaging was conducted 24 h post-injection, followed by weekly intervals post-administration for 30 days with the region of interest (ROI) analyzed via luminescence or photon counts compared to the control group. At the end of the study, animals were euthanized as approved by IACUC using an overdose of carbon dioxide followed by cervical dislocation. Afterwards, hind limbs were harvested for analysis[52].

Bone densitometry
Bone density was measured prior to the intratibial injection and termination of experiments by dual emission x-ray absorptiometry (DEXA) on a Lunar PIXImus scanner (GE Healthcare, Chicago, IL) as per a previous procedure[53]. Briefly, each mouse was weighed and anesthetized with 2% inhaled isoflurane vapor and then placed onto the PIXImus platform where they received a 5-minute DEXA scan. Analysis performed using PIXImus software (GE Healthcare) provided quantification of bone mineral density (BMD) and bone mineral content (BMC) of the injected and un-injected tibia. DEXA data is presented using a ratio of BMD or BMC parameters acquired from the injected tibia (left) versus the un-injected tibia (right) of each mouse.

Micro-CT analysis
The hind limbs (tibiae and femora) were harvested and fixed in 4% paraformaldehyde for 48 h at 4 °C. The bones were then transferred to 70% ethanol and stored in 4 °C until further analysis. Using SkyScan 1273 high-resolution micro-computed tomography (μCT, Bruker, Billerica, MA) connected to a Hamamatsu L9181-02 camera, high-resolution scanning was performed on the left tibiae at the following settings: 80 kV, 100 μA, detection pixel of 9 μm, and 0.5 mm aluminum filter with 2 images captured at every 0.5° through 180° rotation. The tibia images were reconstructed using SkyScan NRecon software and quantified using the Bruker CT analysis (CTan) software. The following trabecular parameters were assessed 0.25 mm below the growth plate at 2.5 mm height[38]: trabecular number (Tb. N), thickness (Tb. Th), separation (Tb. Sp.) and percent bone volume (% BV/TV). The bone and trabecular structure of the control and treated groups were reconstructed three dimensionally using Bruker CTVox and CTvol software, respectively.

Histological analysis of bone sections
The isolated tibiae were decalcified using 10% EDTA (pH 7.4) in dynamic conditions at 4 °C. After 3 days, once the bones were confirmed for reduced stiffness, they were processed using a Leica ASP300S Tissue Processor and embedded in paraffin wax using a Leica HistoCore Arcadia H embedding system (Leica, Wetzlar, Germany). The paraffin blocks were sectioned at 5 μm thickness and were deparaffinized and rehydrated through xylene, graded ethanol, and distilled water, followed by a 2-hour incubation with TRAP stain at 37 °C. After incubation, the slides were rinsed with distilled water, counterstained with 0.02% fast green for 1 min, and rinsed with distilled water several times. The slides were then air dried, cover slipped with DPX mounting medium (Electron Microscopy Sciences, Hatfield, PA), and imaged using an Olympus BX61VS slide scanner (Olympus Life Sciences, Waltham, MA)[54]. The OCs in the bone sections appeared pink to red in color and the background held a green coloration.

Data analysis
We applied GraphPad Prism 6 (GraphPad Software, La Jolla, CA) for statistical analysis and data presentation. Group means were analyzed for normality using a Shapiro-Wilk test and once normality was confirmed with all the variables, we analyzed the datasets with one-way ANOVA with Dunnett's, Sidak's, and/or Tukey's post-hoc tests applied for multiple comparisons. Significance was assessed at a p-value of $p < 0.05$. The fold change and p-values for proteomic data were calculated in Microsoft Excel and plotted using GraphPad Prism.

Results
Effects of LC-OC interaction on OC differentiation and function
We conducted the initial LC-OC interaction studies by differentiating pre-OC cells (RAW 264.7) in the bottom compartment of transwell inserts while LC cells were cultured in the top compartment (LC-OC co-culture). A panel of four LC cell lines consisting of A549, H1437, SK MES-1 and Calu-6 were co-cultured with differentiating OCs. We observed a marked increase in OC differentiation based on TRAP activity especially for OCs cultured with H1437 and SK MES-1 (Fig. 1a, $p < 0.01$). Compared to positive control with RANKL treatment alone, the number of matured OCs ($\geq$ 3 nuclei) was also significantly higher with LC-OC co-culture, especially with H1437 ($p < 0.001$) and A549 cells ($p < 0.01$) (Supplemental Fig. S1a). We proceeded to count the size of the multinucleated OCs (matured OCs) judging by the number of nuclei. We observed a significant increase in the number of large OCs (nuclei > 10) in LC-OC co-culture with A549 ($p < 0.0001$), H1437 ($p < 0.0001$), SK MES-1 and Calu-6 ($p < 0.05$) when compared to RANKL alone (Fig. 1b-c). Assessment of bone resorption was conducted by differentiating OCs on bovine bone slices in the bottom compartment of the transwell inserts while LC cells were cultured on the top compartment. Our results showed that LC-OC co-culture significantly facilitated the extent of bone resorption by OCs among all LC cell lines compared to RANKL treatment alone: (Calu-6; $p < 0.05$), (SK MES-1 and A549; $p < 0.01$), and (H1437; $p < 0.0001$) (Fig. 1d-e). The increase in area of resorption followed this order: H1437 > A549 $\geq$ SK MES-1 > Calu-6 (Fig. 1d-e).

Subsequent LC-OC interaction was simulated by treating differentiating OCs with LC-CM. With LC-CM treatment, we observed an increase in OC differentiation based on TRAP activity that was significant with SK MES-1-CM and Calu-6-CM when compared to the RANKL alone (Fig. 2a; $p < 0.01$). In addition, LC-CM
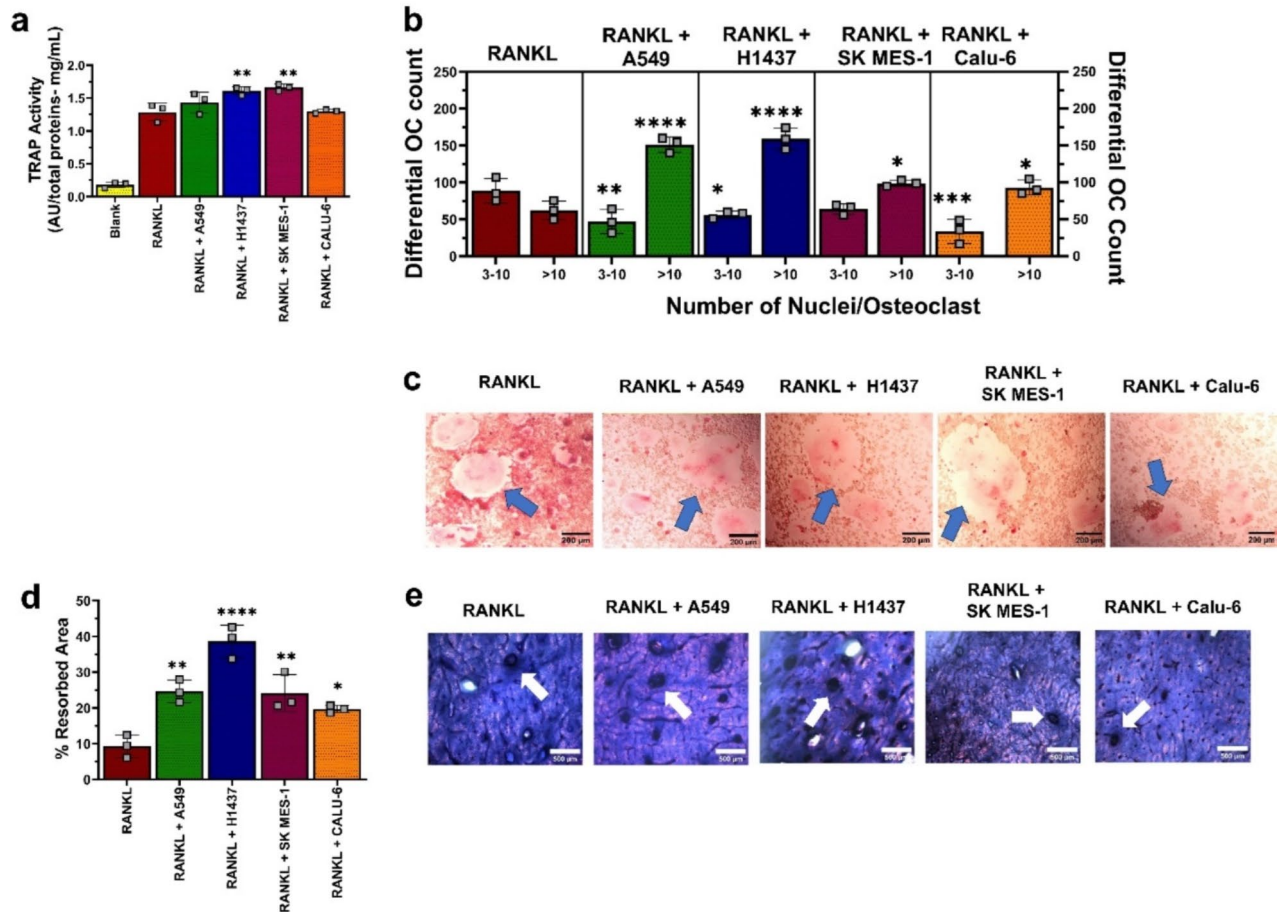
Fig. 1. LC-OC interaction facilitated OC differentiation and function. A panel of LC cells were co-cultured with RAW 264.7 cells (pre-OC) cells and differentiated to matured OCs. The extent of OC differentiation was measured via **(a)** TRAP activity and **(b)** number of matured TRAP-stained multinucleated OCs according to the nuclei: 3–10 or > 10. **(c)** Representative images of TRAP-stained multinucleated OCs (blue arrows). Each data point represents mean $\pm$ SD ($n = 3$). Scale bar = 200 μm. **(d)** Percentage of resorbed area for OC differentiation carried out on bovine bone slices. **(e)** Representative images of osteoclastic resorptive pits (white arrows) on bovine bone slices stained with toluidine blue. Each data point represents mean $\pm$ SD ($n = 3$); *$p < 0.05$, **$p < 0.01$, ***$p < 0.001$, ****$p < 0.0001$ vs. RANKL (positive control cells without LC co-incubation). Scale bar = 500 μm.

treatments did not negatively affect the fold change from MTT data when compared to untreated control cells (Supplemental Fig. S2a). The OC count (≥ 3 nuclei) showed a slight increase across LC-CM treatments with a significant trend observed only in the wells treated with H1437-CM (Supplemental Fig. S2b; $p < 0.05$). Results from the differential OC count (according to number of nuclei) showed a high number of large OCs (nuclei > 10) with LC-CM treatment that was pronounced with H1437-CM ($p < 0.001$) and SK MES-1-CM ($p < 0.01$) compared to RANKL alone (Fig. 2b-c). Assessment of OC function was conducted by differentiating OCs with LC-CM treatments on bovine bone slices. We observed a remarkable increase in the percentage of resorbed area with treatment of differentiating OCs with A549-CM ($p < 0.001$), H1437-CM ($p < 0.0001$) and SK MES-1-CM ($p < 0.001$) (Fig. 2d-e).

To establish the influence of LC-derived EVs in LC-OC interaction, we applied LC-Exo in OC differentiation studies. We used exosomes derived from BEAS-2b (BEAS-2b-Exo) as a control. The isolated exosomes were characterized by DLS (Fig. 3a) with average sizes of 120.6 ± 10 nm (BEAS-2b-Exo), 83.2 ± 5.9 nm (A549-Exo), 107.5 ± 12 nm (H1437-Exo), 114.9 ± 12 nm (SK MES-1-Exo) and 111.5 ± 23 nm (Calu-6-Exo). TEM micrographs showed that A549-Exo appeared spherical in shape with around 100 nm diameter (Fig. 3b). In all, LC-Exo samples were validated by TEM and western blotting analysis for exosome markers such as ALIX, TSG 101 and CD63 using β-actin as a positive control for their counterpart cell lysates (Fig. 3b-c and Supplemental Fig. S3a-b). LC-Exo treatment did not cause a pronounced increase in TRAP activity (Fig. 3d) as well as OC count (≥ 3 nuclei) (Supplemental Fig. S3c) versus RANKL alone group. There was a slight increase in the number of matured OCs (with nuclei > 10) (Fig. 3e-f). MTT assay showed that LC-Exo treatments did not cause detectable negative changes when compared to untreated control cells (Supplemental Fig. S3d). Interestingly, results from the resorption assay showed a pronounced increase in the percentage of bone resorbed area with
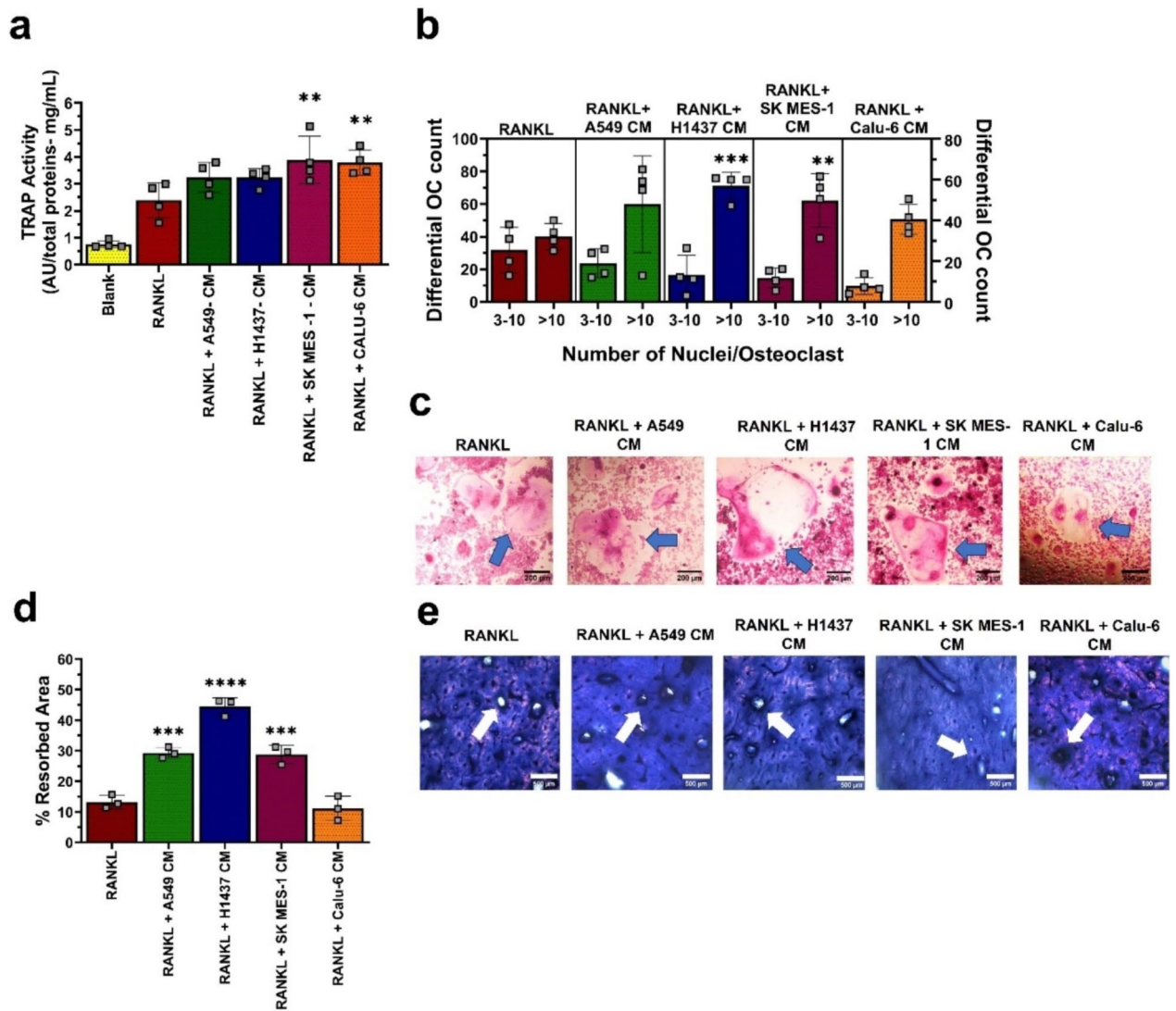
Fig. 2. LC-CM treatment influenced OC differentiation and function. CM from a panel of LC cells were treated with pre-OCs (RAW 264.7 cells). The extent of OC differentiation was measured via **(a)** TRAP activity, **(b)** differential count of TRAP-stained matured OCs according to the number of nuclei: 3–10 or > 10 and **(c)** representative images of TRAP-stained multinucleated OCs (blue arrows). Each data point represents mean ± SD ($n = 4$). Scale bar = 200 μm. **(d)** Percentage of resorbed area for OC differentiation carried out on bovine bone slices with various LC-CM treatments. **(e)** Representative images of osteoclastic resorptive pits (white arrows) on bovine bone slices stained with toluidine blue. Each data point represents mean ± SD ($n = 3$); **$p < 0.01$, ***$p < 0.001$, ****$p < 0.0001$ vs. RANKL (positive control cells). Scale bar = 500 μm.

LC-Exo treatments versus the RANKL alone group in the following order: A549-Exo ($p < 0.0001$), H1437-Exo ($p < 0.0001$), SK MES-1-Exo ($p < 0.01$) and Calu-6-Exo ($p < 0.05$) (Fig. 3g-h).

Characterization and identification of proteins in LC-Exo

We paid particular attention to protein content within LC-Exo and assessed their potential contribution to LC-OC interaction. Using proteomic tools, we analyzed the protein content within LC-Exo in comparison to BEAS-2b-Exo and plotted their changes in regulation levels via volcano plot (Fig. 4a-d). We observed that Gal3bp expression was significantly upregulated by 2.02 and 3.24 log 2-fold change in A549- and SK MES-1-Exo, followed by a 1.5-log fold change in Calu-6-Exo while the expression of Gal3bp in H1437-Exo was not markedly higher than in BEAS-2b-Exo (Fig. 4a-d). Comparatively, we observed that 13 exosomal proteins were common among the panel of LC cells (Supplemental Fig. S4a), with the heat map showing a potential elevation (compared to BEAS-2b-Exo) of key proteins in LC-Exo such as retinol-binding protein, apolipoprotein M, microtubule-associated protein, and Gal3bp (Fig. 4e). Further, gene ontology[55] was performed to analyze exosomal proteins depicted in the volcano plot using a molecular function of the gene that matched with "protein binding" (Supplemental Fig. S4b). Cellular component analysis (Supplemental Fig. S4c) showed the Gal3bp gene
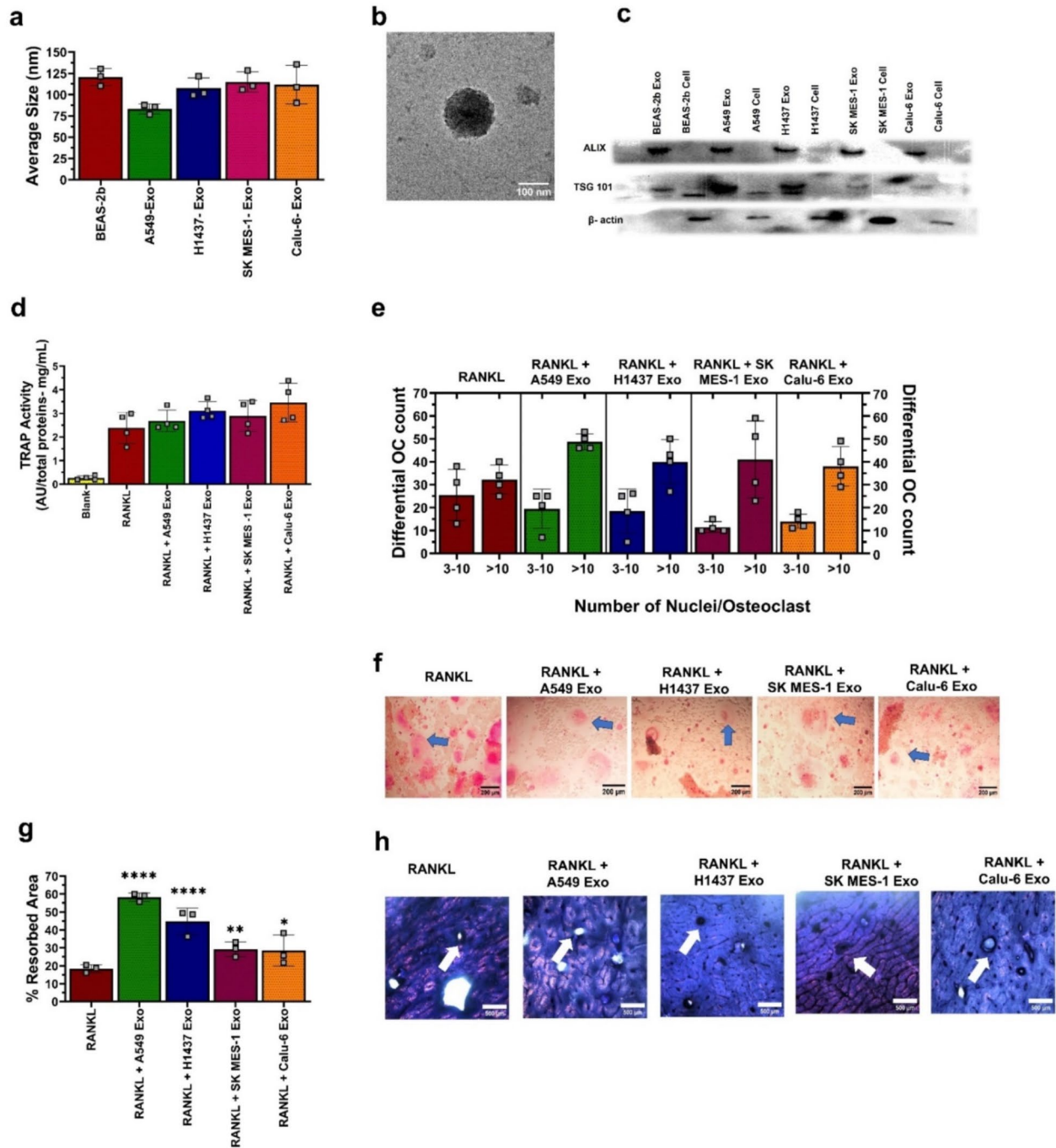
Fig. 3. LC-Exo characterization and effects on OC differentiation and function. LC-Exo samples were isolated and characterized using **(a)** DLS to determine average size ($n = 3$). **(b)** TEM imaging using negative staining for A549-Exo. Scale bar = 100 nm. **(c)** Western blotting analysis of exosomal markers ALIX and TSG 101 with β-actin as a loading control. Each data point represents mean ± SD ($n = 3$). LC-OC interaction via LC-Exo treatment was assessed via **(d)** TRAP activity and **(e)** OC differential count according to the number of nuclei: 3–10 or > 10, with **(f)** representative images of the extent of TRAP-staining in OCs (blue arrows). Each data point represents mean ± SD ($n = 4$). Scale bar = 200 μm. **(g)** Percentage of resorbed area for OCs differentiated on bone slices and treated with LC-Exo with **(h)** representative images of resorptive pits (white arrows) on bone slices stained with toluidine blue. Each data point represents mean ± SD ($n = 3$); *$p < 0.05$, **$p < 0.01$, ****$p < 0.0001$ vs. RANKL (positive control cells). Scale bar = 500 μm.
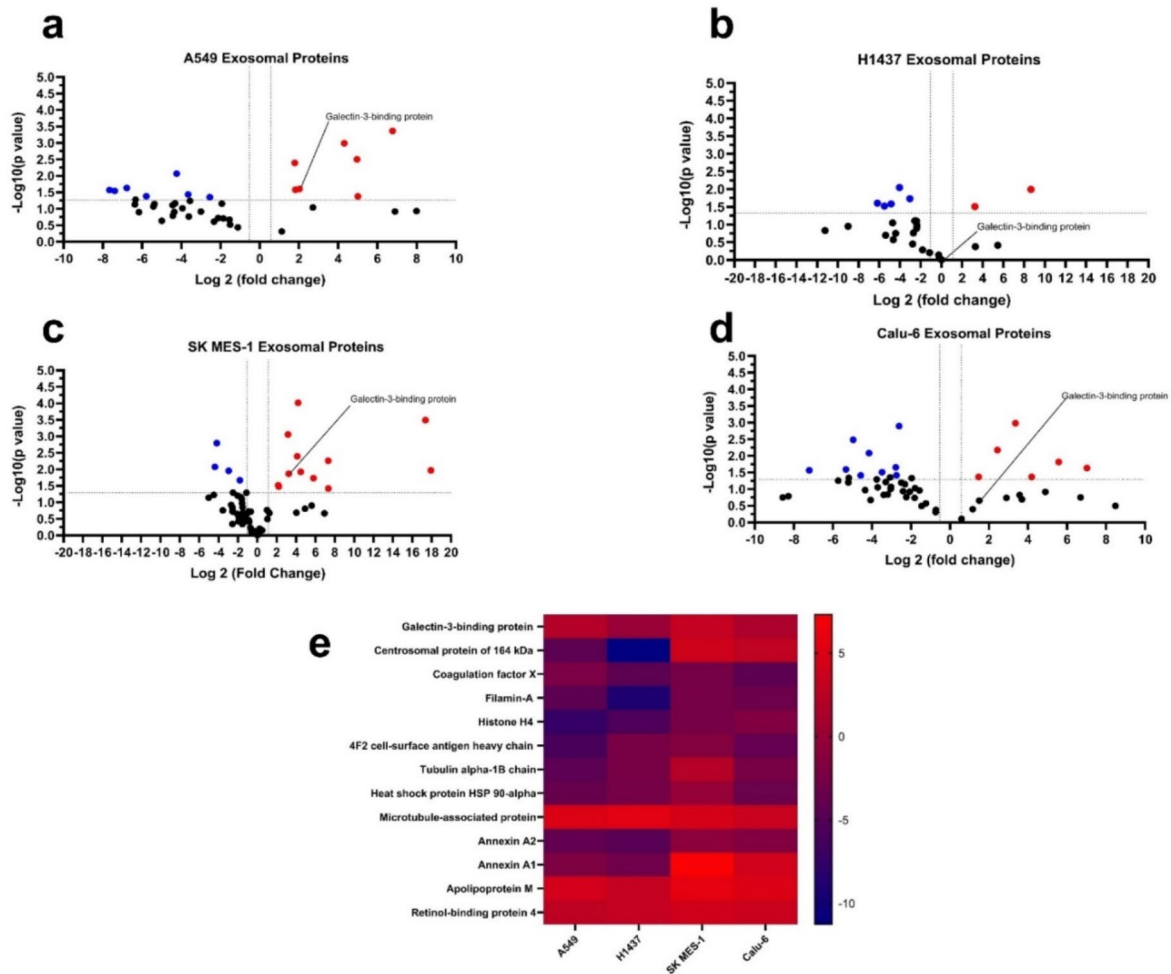
Fig. 4. Proteomic analysis identified Gal3bp in LC-Exo samples. LC-Exo samples were compared to BEAS-2b-Exo in proteomic analysis via LC-MS/MS. The normalized exosomal proteins of **(a)** A549, **(b)** H1437, **(c)** SK MES-1 and **(d)** Calu-6 were plotted via volcano plots where red and blue dots represent the statistically up- and down-regulated proteins. Each data point represents mean ± SD ($n=3$; $p<0.05$). **(e)** Heat map of 13 common exosomal protein expression levels from the LC panel of cells, where blue and red represent low and high protein expression respectively.

distributed in the following components: (i) collagen containing extracellular matrix, (ii) extracellular exosomes, (iii) extracellular region, (iv) extracellular space and (v) cell membrane.

Focusing on Gal3bp, we conducted further analyses using an automated western blot system (JESS) and obtained the following results: (i) Gal3bp expression was significantly higher within all LC-Exo except H1437-Exo, which had a significantly lower Gal3bp concentration compared to BEAS-2b-Exo (Fig. 5a; $p<0.0001$). (ii) Gal3bp expression levels within LC-Exo were found to be markedly higher than LC lysates according to the following: 51 times (A549), 10 times (H1437), 13 times (SK MES-1) and 14 times (Calu-6) (Fig. 5a-b). The representative blot images displaying Gal3bp expression levels across LC-Exo and cell lysates are shown (Fig. 5c-d). Results from ELISA supported the western blotting analysis in that LC-Exo showed significantly higher Gal3bp concentrations than in LC cell lysates (Fig. 5e; Calu-6- $p<0.01$, SK MES-1- $p<0.001$, A549- $p<0.0001$).

In a separate study, we evaluated the levels of galectin 3 (Gal3) in LC-Exo and LC cell lysates. It has been reported that Gal3bp's multifaceted nature enables interaction with multiple binding partners which subsequently will influence the signaling pathways[32]. Previous studies recognized Gal3 as a common binding partner of Gal3bp in breast cancer progression and invasion[32]. Using automated western analysis (JESS), we observed that Gal3 expression levels were significantly decreased ($p<0.0001$) in LC-Exo when compared to BEAS-2B-Exo (Supplemental Fig S5a-d). Among all LC cell lines, the expression level of Gal3 was significantly higher ($p<0.05$) in LC cell lysates than in the respective LC-Exo (Supplemental Fig S5a-d).

Mechanistic assessment of LC-OC interaction
We conducted a series of western blot analyses on differentiating OCs during LC-OC co-culture. We evaluated expression levels of the following markers: NFAT2, TRAF6, p-44/42 MAPK, and p-SAPK/JNK (Fig. 6). OCs
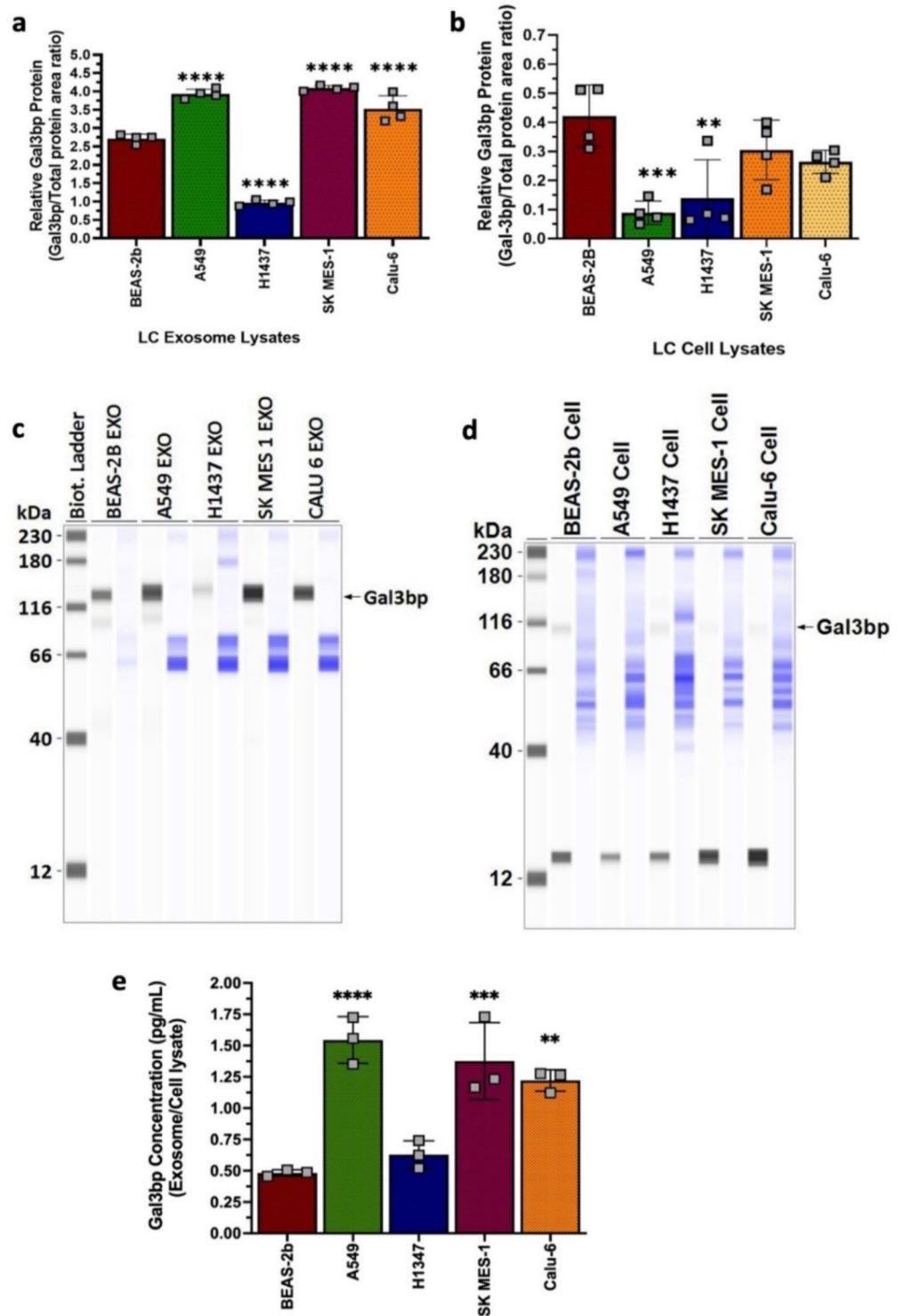
Fig. 5. Characterization of Gal3bp expression in LC-Exo and LC Cell lysates. Using JESS protein simple system, LC-Exo and cell lysates were measured for protein expression of **(a-b)** Gal3bp with **(c-d)** representative blots showing Gal3bp (black) and total protein (blue) as a loading control. Each data point represents mean $\pm$ SD ($n = 4$). **(e)** The ratio of Gal3bp concentration detected within LC-Exo to their respective cell lysates is depicted to assess the difference between each cell line. Each data point represents mean $\pm$ SD ($n = 3$); $^{**}p < 0.01$, $^{***}p < 0.001$, $^{****}p < 0.0001$ vs. BEAS-2b.
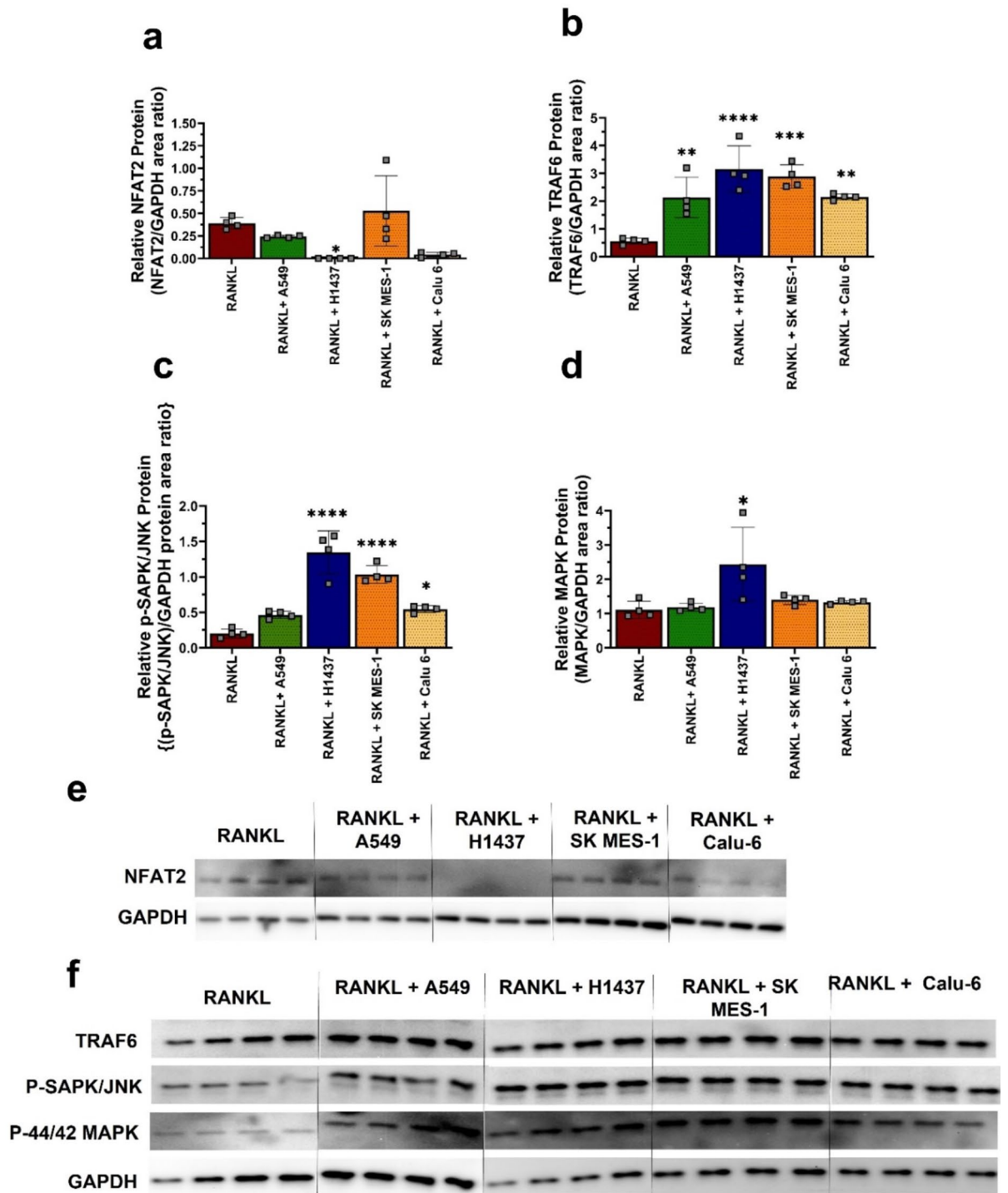
Fig. 6. Mechanistic assessment of OCs in LC-OC interaction. Differentiated OCs alone or co-incubated with LC cells were lysed after the second treatment of RANKL (day 4) to assess any changes in the expression levels of critical markers via western blot. The immunoblots were analyzed using ImageJ and plotted for the following markers: **(a)** NFAT2, **(b)** TRAF6, **(c-d)** p-44/42 MAPK, and p-SAPK/JNK using GAPDH as loading control with **(e-f)** representative blots shown. Each data point represents mean $\pm$ SD ($n = 4$); $*p < 0.05$, $**p < 0.01$, $***p < 0.001$, $****p < 0.0001$ vs. RANKL.

co-cultured with H1437, A549, and Calu-6 showed a decrease expression of NFAT2 (Fig. 6a, $p < 0.05$) which has been reported to be a key transcription factor in OC differentiation[56] Additionally, a significant increase in TRAF6 expression was observed within OCs co-cultured with H1437 ($p < 0.0001$), SK MES-1 ($p < 0.001$), A549 ($p < 0.01$) and Calu-6 ($p < 0.01$) (Fig. 6b). TRAF6 is another crucial marker which is recruited upon conformational binding of RANKL to the RANK receptor for activating the MAPK pathway, one of the many signaling pathways involved in OC differentiation[57,58]. Interestingly, we saw a significant increase ($p < 0.05$) in the p-44/42 MAPK expression within OCs co-cultured with H1437, however OCs co-cultured with other LC cells did not show detectable changes compared to RANKL (Fig. 6c-d). Analysis of p-SAPK/JNK, a phosphorylated protein involved in RANKL mediated-OC formation[59], showed increased expression within OCs co-cultured with H1437 ($p < 0.0001$), SK MES-1 ($p < 0.0001$) and Calu-6 ($p < 0.05$) (Fig. 6 c-d). Images of the blots for NFAT2, TRAF6, p-44/42 MAPK, p-SAPK/JNK and GAPDH are shown (Fig. 6e-f). cFos is an essential marker involved in differentiation of macrophages to OCs, we observed a slight decrease in its expression levels among all OC co-culture with LC cells (Supplemental Fig S6a). We also evaluated the expression of TRAP, which is known to regulate bone development and growth[60], and observed no detectable difference in the expression within the LC-OC co-culture (Supplemental Fig S6b). Further studies assessed other markers that are involved in the fusion process of mononuclear pre-OCs resulting in matured multinucleated OCs such as DC-Stamp and CD9[61]. The expression levels of DC-Stamp in OCs from LC-OC co-culture were comparable to RANKL alone except for a decrease which was more pronounced with Calu-6 ($p < 0.0001$) than with SK MES-1 ($p < 0.05$) (Supplemental Fig S6c). In contrast, there was a significant increase in CD9 expression within OCs co-cultured with H1437 ($p < 0.0001$), SK MES-1 ($p < 0.05$), and Calu-6 ($p < 0.01$) (Supplemental Fig S6d). Images of the blots for cFos, TRAP, DC-Stamp, and CD9 are shown (Supplemental Fig. S6e-f).

Effect of Gal3bp on OC differentiation and function
We conducted additional studies using rGal3bp to assess the effect of the marker towards differentiating OCs and their respective function (Fig. 7). At rGal3bp concentrations ranging from 5 to 25 ng/mL, we observed a significant increase in OC differentiation based on TRAP activity (Fig. 7a; $p < 0.01$). Prior to the studies, we confirmed that rGal3bp did not have detectable negative changes to pre-OCs via MTT assay (Supplemental Fig S7a). The effects of rGal3bp on OC count (≥ 3 nuclei) was not pronounced with a slight increase at 25 ng/mL (Fig. 7b-c, $p < 0.05$). Interestingly, we observed a concentration-dependent increase in the resorbed bone area when differentiating OCs were treated with rGal3bp (Figs. 7d-e and 25 ng/mL $p < 0.001$, 50 ng/mL $p < 0.0001$).

To assess the impact of Gal3bp on enhanced osteoclastogenesis, a comparative study was undertaken by treating differentiating OCs with anti-Gal3bp (10 μg/mL) alone or in conjunction with A549-Exo or rGal3bp (25 ng/mL, Fig. 7f-g). MTT assay of pre-OCs showed no detectable changes with anti-Gal3bp treatment from concentrations ranging from 0.07 to 1.25 μg/mL (Supplemental Fig. S7b). Further, there was no significant changes to TRAP activity with the addition of anti-Gal3bp treatment to RANKL or A549-Exo (Supplemental Fig. S7c). Interestingly, we observed a concentration-dependent increase in the resorbed bone area when differentiating OCs were treated with rGal3bp (Figs. 7d-e and 25 ng/mL; $p < 0.001$, 50 ng/mL; $p < 0.0001$). It is also noted that treatment with rGal3bp was comparable to A549-Exo with a significant increase in OC count (≥ 3 nuclei). (Fig. 7f; $p < 0.0001$). Interestingly, we observed a remarkable reduction in OC count (≥ 3 nuclei) when anti-Gal3bp was added to all treatment groups such as RANKL ($p < 0.01$), A549-Exo ($p < 0.0001$) and rGal3bp ($p < 0.0001$) (Fig. 7f-g). Additionally, immunoblot analysis of the OC lysates revealed a significant decrease in p44/42 MAPK expression in the wells treated with anti-Gal3bp (Supplemental Fig. S7d-e, $p < 0.05$, $p < 0.01$).

In-vivo assessment of the effects of Gal3bp on LC interaction with bone tissues
In accordance with IACUC approval, we selected A549 as a representative cell line for intratibial injections of LC cells in athymic mice (nu/nu) with the opportunity to assess LC-OC interaction in an in-vivo setting. As such, A549-Luc2 cells were injected into the tibiae of athymic (nu/nu) mice with or without exogeneous supplementation of rGal3bp (25 ng/mL). The extent of tumor development as monitored via bioluminescent imaging showed a gradual increase ($p > 0.05$) in luminescence intensity until 21 days post-injection, followed by a plateau stage until termination (Fig. 8a-b). The data acquired on day 21 post-injection indicated that intra-tibial injection of A549-Luc2 cells with rGal3bp had the highest bioluminescence compared to the group that received A549-Luc2 cells alone (Fig. 8b). Compared to untreated control mice, DEXA analysis did not show detectable changes in bone mineral density (BMD) (Supplemental Fig S8a). There was a decrease in bone mineral content (BMC) compared to untreated control mice only in mice that received A549-Luc2 without rGal3bp supplementation (Supplemental Fig. S8b; $p < 0.05$).

The isolated tibiae were subjected to μCT scanning, reconstruction, and analysis to assess the alteration in the skeletal morphology. Analysis from CTan software revealed that intratibial injection of A549-Luc2 cells with rGal3bp supplementation caused a minimal increase in the trabecular separation, a significant decrease in the trabecular number ($p < 0.05$) and a pronounced reduction in bone volume ($p < 0.001$, $p < 0.01$, $p < 0.05$) (Fig. 8c-e). Further analysis of the 3D reconstructed μCT data showed extensive damage to the skeletal architecture with intratibial injection of A549-Luc2 cells and the trend was pronounced with rGal3bp supplementation (Fig. 8g-h). We also observed altered or distorted trabecular structure among the groups that received A549-Luc2 cells with or without rGal3bp supplementation compared to untreated control mice (Fig. 8f-h). Further, histological staining of bone sections via TRAP showed that OCs were visualized near the epiphysis only for untreated control mice (Fig. 8f). Meanwhile, bone sections from the groups that received A549-Luc2 cells with or without rGal3bp supplementation showed an overstimulated OC presence as depicted by TRAP staining throughout the bone structure (Fig. 8g-h). In a separate study, we confirmed that mice that received intratibial injection of rGal3bp alone (25 ng/mL) without A549-Luc-2 cells did not show any noticeable changes to their bone
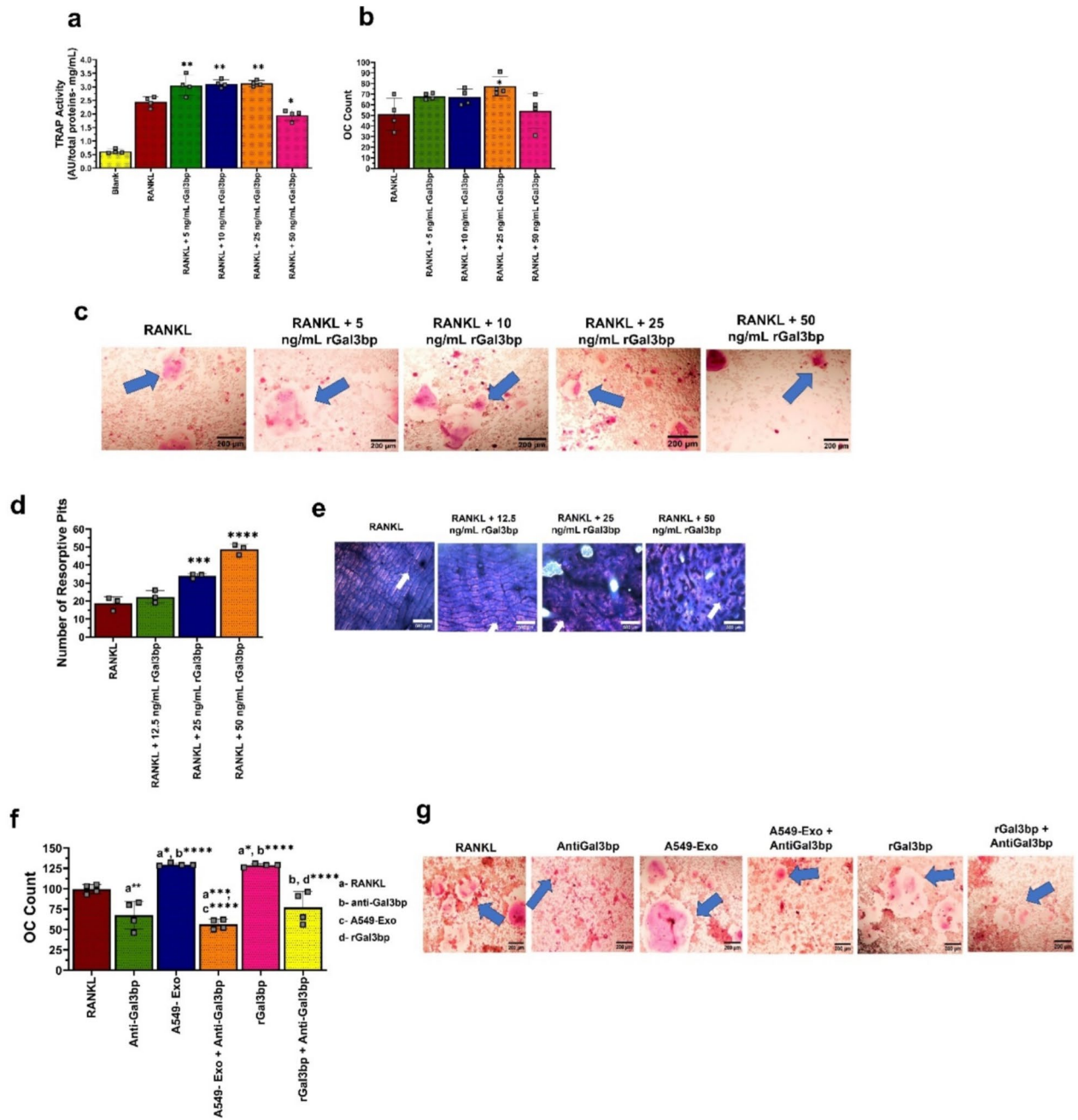
Fig. 7. Recombinant Gal3bp promoted OC differentiation and function. Different concentrations of rGal3bp were exposed to differentiating OCs. The extent of OC differentiation was assessed by **(a)** TRAP activity and **(b)** OC count with **(c)** representative images of the TRAP-stained multinucleated OCs (blue arrows). Each data point represents mean $\pm$ SD ($n = 4$). Scale bar $= 200\ \mu m$. Pre-OC cells seeded onto bone slices were treated with rGal3bp and the extent of OC resorption was assessed by **(d)** the percentage of resorbed area with **(e)** representative images of resorptive pits (white arrows) on bone slices stained with toluidine blue. Each data point represents mean $\pm$ SD ($n = 3$); *$p < 0.05$, **$p < 0.01$ ***$p < 0.001$, ****$p < 0.0001$ vs. RANKL. Scale bar $= 500\ \mu m$. The extent of OC differentiation when treated with anti-Gal3bp alone or in combination with A549-Exo or rGal3bp was assessed by **(f)** OC count with **(g)** representative images of the TRAP-stained multinucleated OCs (blue arrows). Each data point represents mean $\pm$ SD ($n = 4$); *$p < 0.05$, **$p < 0.01$, ***$p < 0.001$, ****$p < 0.0001$ vs. [a]RANKL, [b]anti-Gal3bp, [c]A549-Exo or [d]rGal3bp. Scale bar $= 200\ \mu m$.
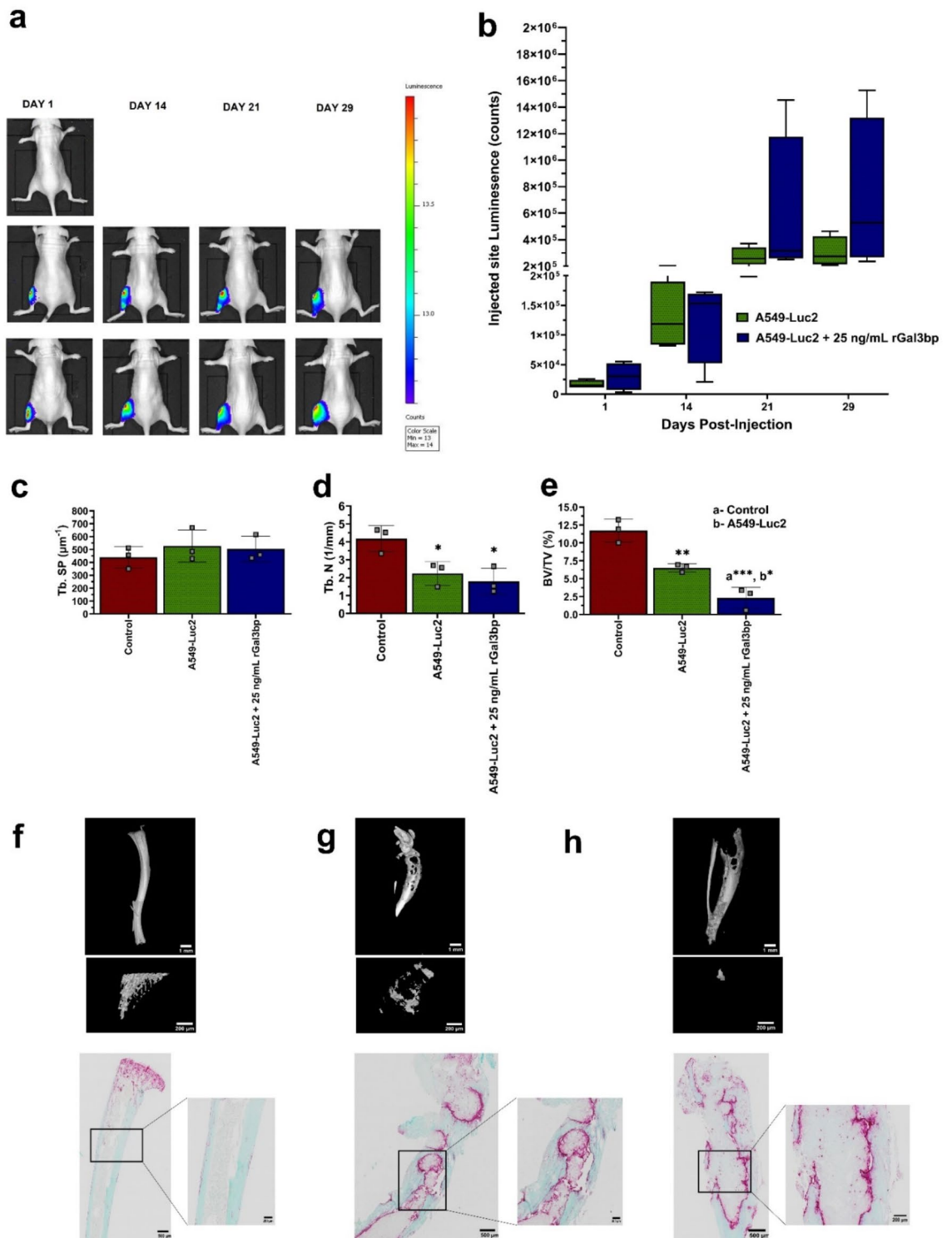
parameters when compared to untreated control mice (Supplemental Fig. S9). This was based on the following assessments: DEXA, μCT and TRAP staining of bone sections (Supplemental Fig. S9a-g).

Discussion

Comprehension of the interaction between LC and bone cells is vital to the development of effective therapeutic strategies for osteolytic metastasis[62,63]. Our primary method of investigating LC-OC interaction was through the co-culture of LC cells (top compartment) and differentiating OCs (bottom compartment) through transwell inserts[64]. We selected a panel of four LC cells to help in aligning our observations with the heterogeneous nature of LC knowing that the selected panel of LC cells does not cover all the numerous subtypes of LC. At this stage of our studies, we did not apply LC-OC mixed culture (in the same wells) setting due to the need to examine the impact of LC secretomes on the OC differentiation process without the interference that a mixed culture could

◀**Fig. 8**. Enhancement of osteolytic lesions following intra-tibial injection of A549 cells with rGal3bp supplementation. Athymic mice (nu/nu) were divided into the following according to: (i) untreated control that did not receive intratibial injection of A549-Luc2 cells, (ii) intra-tibial injection of A549-Luc2 cells and (iii) intra-tibial injection of A549-Luc2 cells with 25 ng/mL rGal3bp supplementation. **(a)** The mice were subjected to bioluminescent imaging on a weekly basis for 30 days. The extent of tumor growth was assessed via **(b)** the resultant luminescence photon count. Each data point represents mean ± SD ($n = 4$ mice). After 30 days post-injection, the tibiae were harvested and subjected to μCT scanning, followed by 2D reconstruction. The extent of trabecular damage between the groups was assessed for the following: **(c)** trabecular separation **(d)** trabecular number and **(e)** percent bone volume/tissue volume. 3D images of the following groups are presented as **(f)** control, **(g)** A549-Luc2 cells and **(h)** A549-Luc2 cells supplemented with 25 ng/mL rGal3bp (Scale bar = 1 mm). Trabeculae of the respective tibia were reconstructed using CTvol for each group (Scale bar = 200 μm). Histological sections of the isolated tibiae were subjected to TRAP staining to identify OCs and counterstained with fast green (Scale bar = 500 and 200 μm). Each data point represents mean ± SD ($n = 3$); *$p < 0.05$, **$p < 0.01$, ***$p < 0.001$ vs. control or A549-Luc2.

pose. While LC-OC co-culture facilitated OC differentiation and function across the LC cells studied, LC-CM and LC-Exo treatments showed varying effects on TRAP activity comparable to the RANKL alone treatment group. This is possibly due to the fact the LC-CM and LC-Exo treatments were applied at one concentration level. The challenge of using one concentration level can also be viewed from the fact that LC secretomes are expected to have variability in the biomolecular content due to the heterogeneous nature of LC[65]. Thus, additional follow-up studies using varying concentrations of LC-CM or LC-Exo in treating differentiating OCs would be beneficial. Interestingly, as in LC-OC interaction via co-culture, OC treatment with LC-CM or LC-Exo caused a remarkable production of large-sized OCs (nuclei > 10) which we observed to translate into pronounced bone resorption. Earlier studies which classified OC size distribution into small (3–5 nuclei), medium (6–9 nuclei) and large (> 10 nuclei) and reported a link between large OCs and extensive bone resorption[66].

We proceeded to conduct mechanistic assessment of LC-OC interaction from the co-culture setting. Increasing expression of TRAF6, p44/42 MAPK, CD9, and p-SAPK/JNK expressions in OCs co-cultured with LC cells, combined with a decrease expression in the crucial OC differentiation factor NFAT2[67], suggests that LC-OC interaction most likely caused an alternative OC differentiation pathway that supported OC production. In addition, OC markers such as DC-Stamp and CD9 have been reported to be among key regulators in the fusion process of mononuclear pre-OCs to produce multinucleated matured OCs[68]. Blotting analysis showed no elevation of DC-Stamp (compared to positive controls with RANKL treatment alone) in the LC-OC interaction studies except a decrease expression level in Calu-6. Meanwhile, CD9 was shown to be significantly upregulated within OCs in the LC-OC co-culture with H1437, SKMES-1 and Calu-6. It is likely that the increased OC size, OC count and function could be attributed to increased fusion of the mononuclear OCs at an early stage of osteoclastogenesis. In addition, correlation between NFAT2, CD9 and DC-stamp expression has been shown to play a pivotal role in OC fusion, where activation of NFAT2 was linked to cell fusion, differentiation and resorption[69–71]. It should be noted that we analyzed NFAT2 from a whole cell lysate sample and that follow-up studies will benefit from analyzing its cytoplasmic and nuclear expression levels. In our work, a decrease in NFAT2 expression and an increase in CD9 and MAPK expression could suggest that LC cells promoted OC differentiation and function by potentially upregulating mononuclear pre-OC cell fusion capability via an alternative MAPK-regulated transcription factor.

In an attempt to identify potential biomolecules that possibly contributed to LC-OC interaction, we paid particular attention to LC-Exo. Exosomes play crucial roles in trafficking various biomolecules for cell communications and have been shown to promote the proliferative and metastatic nature of LC[72]. Also, it has been reported that exosomes derived from LC contain cargos of biomolecules that can influence the phenotype and genotype of the recipient cells[73]. The isolated exosomes from our panel of LC cells initially were characterized by size (DLS and TEM) and western blotting analyses for key exosomal markers. We identified Gal3bp from proteomic analyses of LC-Exo samples. We were intrigued by earlier studies that reported high expression levels of Gal3bp in a various cancers such as pancreatic[33], neuroblastoma[74], endometrial[75], breast[32] and lung cancer[76]. Results from additional studies with rGal3bp and anti-Gal3bp supported the trend from this work that rGal3bp potentially promoted OC differentiation and function. The bone resorptive effects of rGal3bp and LC-Exo were suppressed markedly with anti-Gal-3 bp treatments. The reduction in p42/44-MAPK protein expression in wells treated with anti-Gal3bp further suggests that Gal3bp may likely regulate OC differentiation through the MAPK pathway. Further studies will be needed to understand gene and protein expression levels for all the OC markers at different time points during OC differentiation during LC-OC interaction. It may also be necessary to apply human primary cell cultures to fully clarify the molecular pathways that are involved in Gal3bp's effect on osteoclastogenesis.

LC-Exo samples showed significantly high concentrations of Gal3bp compared to their respective LC-CM and LC cell lysates, which suggests that Gal3bp was largely secreted via LC-Exo. This trend agrees with earlier studies on glioblastoma, that demonstrated that Gal3bp could be transported through cancer extracellular vesicles[77]. However, the role of Gal3bp in BM of cancer has not been elucidated which supported the premise for this work.

To investigate the possible roles of LC-exosomal-Gal3bp in BM, we selected A549 as a representative LC cell in accordance with IACUC approval. Our rationale for this selection from the panel of LC cells is that A549-Exo showed the highest concentration of Gal3bp that correlated with the largest resorptive area from ex-vivo studies. We simulated in-vivo LC-OC interaction using intratibial injection of A549-Luc2 cells and

monitored tumor growth within the bone tissues. Our intention was to examine the extent to which exogenous supplementation of rGal3bp promotes tumor growth within bone tissues. Within two weeks post-intratibial injection, bioluminescent analysis revealed a significant increase in tumor burden within the tibiae with rGal3bp supplementation. In addition, μCT analysis of the osteo-architecture of the A549-Luc2-injected tibiae showed tremendous destruction of the bone tissue internally and externally as characterized by irregular bone structure. We additionally noted that rGal3bp alone did not alter the osteo-histoarchitecture, however our analysis of A549-Luc2 cells with rGal3bp supplementation suggests that rGal3bp facilitates the ability of A549-Luc2 to influence the OCs within the bone microenvironment, resulting in excessive osseous resorption. While our in-vivo study is supported by assessment of several bone parameters through DEXA, μCT and histology assays, we expect that follow-up studies will assess levels of key markers for bone turnovers/resorption. The extensive bone destruction following intratibial injection of A549-Luc2 cells could also be attributed to the study termination time (30 days), which allowed for extensive tumor growth within the bone tissues. It is likely that a shorter tumor growth time of less than 30 days could offer the opportunity to observe more distinguishing features with rGal3bp supplementation. At 30-days post-injection, we observed a general trend of significant reduction in bone volume with pronounced bone destructive effects with rGal3bp supplementation.

Recent biochemical analysis of Gal3bp revealed that it is a "floating receptor" that binds to other proteins present in intra- and extracellular space and undergoes proteolytic cleavage upon ligand binding[32,35]. It is expected that the potential interaction between Gal3bp and binding partners will be important for its activation and the corresponding signaling pathway could be linked to cancer progression and invasiveness[29]. Gal3 is a notable binding partner for Gal3bp with the potential to influence bone tissues[32]. Our observation indicated that Gal3 is abundantly present in LC cell lysates compared to LC-Exo samples. Interestingly, OCs have been reported to utilize Gal3 to differentiate from their precursor mono-nuclear state to multinucleated bone-resorbing cells[78]. We anticipate that LC-Exo-Gal3bp would possibly interact with Gal3 present within OCs. Previous studies suggested other galectins (Gal 1, 3, or 7) could serve as potential binding partners to Gal3bp with connotations in metastasis of different types of cancers[79]. Additional studies will be needed to fully elucidate the nature and impact of possible interactions between Gal3bp (that we found to be possibly secreted through LC-Exo compared to LC cell lysates) and a prospective binding partner such as Gal3 (that we found to be possibly expressed mainly within the LC cell lysates compared to LC-Exo).

Overall, we found that LC-OC interaction led to enhancement of OC differentiation and function. All LC-OC interaction studies showed a pronounced increase in resorption which could be linked to production of OCs with high numbers of nuclei. Further assessment revealed that the majority of the LC-Exo (A549, SK MES-1 and Calu-6) exhibited high expressions of Gal3bp, which was implicated in facilitating OC differentiation and resorption. Mechanistic assessment of LC-OC interaction supported the enhancement of OC differentiation and potential upregulation of fusion capability of mononuclear pre-OCs to matured OCs. The results from intratibial injection of LC cells supported a potential effect of rGal3bp in facilitating growth of LC within bone tissues thereby causing bone destruction. Follow-up studies are warranted to fully elucidate the roles of LC exosomal Gal3bp in osteolytic metastasis.

Data availability
The datasets generated during and/or analyzed during the current study are available from the corresponding author upon reasonable request.

References
1. Chen, W. C. et al. Bone sialoprotein promotes lung cancer osteolytic bone metastasis via MMP14-dependent mechanisms. *Biochem. Pharmacol.* **211**, 115540 (2023).
2. Brunetti, G. et al. LIGHT/TNFSF14 promotes osteolytic bone metastases in non-small cell lung cancer patients. *J. Bone Miner. Res.* **35**, 671–680 (2020).
3. Teocharoen, R., Ruangritchankul, K., Vinayanuwattikun, C., Sriuranpong, V. & Sitthideatphaiboon, P. Vimentin expression status is a potential biomarker for brain metastasis development in EGFR-mutant NSCLC patients. *Transl Lung Cancer Res.* **10**, 790–801. https://doi.org/10.21037/tlcr-20-1020 (2021).
4. Ding, C. et al. Overexpression of PEAK1 contributes to epithelial–mesenchymal transition and tumor metastasis in lung cancer through modulating ERK1/2 and JAK2 signaling. *Cell Death Dis.* **9**, 802. https://doi.org/10.1038/s41419-018-0817-1 (2018).
5. Zhao, M. N. et al. A novel microRNA-182/Interleukin-8 regulatory axis controls osteolytic bone metastasis of lung cancer. *Cell Death Dis.* **14**, 298 (2023).
6. Wang, M., Xia, F., Wei, Y. & Wei, X. Molecular mechanisms and clinical management of cancer bone metastasis. *Bone Res.* **8**, 30 (2020).
7. Yang, X. et al. Wnt signaling through Snail1 and Zeb1 regulates bone metastasis in lung cancer. *Am. J. Cancer Res.* **5**, 748–755 (2015).
8. Song, X. et al. EGFL6 promotes bone metastasis of lung adenocarcinoma by increasing cancer cell malignancy and bone resorption. *Clin. Exp. Metastasis.* **40**, 357–371. https://doi.org/10.1007/s10585-023-10219-5 (2023).
9. Del Conte, A. et al. Bone metastasis and Immune checkpoint inhibitors in Non-small Cell Lung Cancer (NSCLC): Microenvironment and possible clinical implications. *Int. J. Mol. Sci.* **23**, 6832 (2022).
10. Ni, J. et al. Tumour-derived exosomal lncRNA-SOX2OT promotes bone metastasis of non-small cell lung cancer by targeting the miRNA-194-5p/RAC1 signalling axis in osteoclasts. *Cell Death Dis.* **12**, 662. https://doi.org/10.1038/s41419-021-03928-w (2021).
11. He, Y. et al. IL-20RB mediates tumoral response to osteoclastic niches and promotes bone metastasis of lung cancer. *J. Clin. Invest.* **132** https://doi.org/10.1172/jci157917 (2022).
12. Wu, S., Pan, Y., Mao, Y., Chen, Y. & He, Y. Current progress and mechanisms of bone metastasis in lung cancer: a narrative review. *Translational Lung Cancer Res.* **10**, 439 (2021).

13. Rodríguez, M. et al. Molecular biomarkers in early stage lung cancer. *Transl Lung Cancer Res.* **10**, 1165–1185. https://doi.org/10.21037/tlcr-20-750 (2021).
14. Blanco, M. A. et al. Global secretome analysis identifies novel mediators of bone metastasis. *Cell Res.* **22**, 1339–1355. https://doi.org/10.1038/cr.2012.89 (2012).
15. Fidler, I. J. The pathogenesis of cancer metastasis: the'seed and soil'hypothesis revisited. *Nat. Rev. Cancer.* **3**, 453–458 (2003).
16. Sung, E., Kwon, O. K., Lee, J. M. & Lee, S. Proteomics approach to identify novel metastatic bone markers from the secretome of PC-3 prostate cancer cells. *ELECTROPHORESIS.* **38**, 2638–2645. https://doi.org/10.1002/elps.201700052 (2017).
17. Yang, X. Y., Liao, J. J. & Xue, W. R. FMNL1 down-regulation suppresses bone metastasis through reducing TGF-β1 expression in non-small cell lung cancer (NSCLC). *Biomed. Pharmacother.* **117**, 109126. https://doi.org/10.1016/j.biopha.2019.109126 (2019).
18. She, K., Yang, W., Li, M., Xiong, W. & Zhou, M. FAIM2 promotes non-small cell lung cancer cell growth and bone metastasis by activating the wnt/β-catenin pathway. *Front. Oncol.* **11**, 690142 (2021).
19. Conceição, F. et al. The secretome of parental and bone metastatic breast Cancer elicits distinct effects in Human Osteoclast activity after activation of β2 adrenergic signaling. *Biomolecules.* **13**, 622 (2023).
20. Hung, C. C. et al. Lung cancer cell-derived secretome mediates paraneoplastic inflammation and fibrosis in kidney in mice. *Cancers.* **12**, 3561 (2020).
21. Zhang, J., Fu, B., Li, M. & Mi, S. Secretome of activated fibroblasts induced by exosomes for the discovery of biomarkers in non-small cell lung cancer. *Small.* **17**, 2004750 (2021).
22. Rizwan, M. N. et al. Tumor-derived exosomes: Key players in non-small cell lung cancer metastasis and their implication for targeted therapy. *Mol. Carcinog.* **61**, 269–280 (2022).
23. Zhao, L. et al. Microfluidic-based exosome isolation and highly sensitive aptamer exosome membrane protein detection for lung cancer diagnosis. *Biosens. Bioelectron.* **214**, 114487. https://doi.org/10.1016/j.bios.2022.114487 (2022).
24. Zhang, H. et al. Exosome-delivered EGFR regulates liver microenvironment to promote gastric cancer liver metastasis. *Nat. Commun.* **8**, 15016. https://doi.org/10.1038/ncomms15016 (2017).
25. Zhang, C. et al. Exosomal miR-328 originated from pulmonary adenocarcinoma cells enhances osteoclastogenesis via downregulating Nrp-2 expression. *Cell. Death Discovery.* **8**, 405. https://doi.org/10.1038/s41420-022-01194-z (2022).
26. Wang, M., Zhao, M., Guo, Q., Lou, J. & Wang, L. Non-small cell lung cancer cell–derived exosomal mir-17-5p promotes osteoclast differentiation by targeting PTEN. *Exp. Cell Res.* **408**, 112834. https://doi.org/10.1016/j.yexcr.2021.112834 (2021).
27. Zhang, C. et al. Exosomal lncRNA HOTAIR promotes osteoclast differentiation by targeting TGF-β/PTHrP/RANKL pathway. *Basic Clin. Pharmacol. Toxicol.* **132**, 242–252 (2023).
28. Zhang, X. et al. Increased LGALS3BP promotes proliferation and migration of oral squamous cell carcinoma via PI3K/AKT pathway. *Cell. Signal.* **63**, 109359. https://doi.org/10.1016/j.cellsig.2019.109359 (2019).
29. Capone, E., Iacobelli, S. & Sala, G. Role of galectin 3 binding protein in cancer progression: a potential novel therapeutic target. *J. Translational Med.* **19**, 405. https://doi.org/10.1186/s12967-021-03085-w (2021).
30. Peretz, A. S. R., Rasmussen, N. S., Jacobsen, S., Sjöwall, C. & Nielsen, C. T. Galectin-3-binding protein is a novel predictor of venous thromboembolism in systemic lupus erythematosus. *Clin. Exp. Rheumatol.* **39**, 1360–1368 (2021).
31. Mendes-Frias, A. et al. Galectin-3 binding protein stimulated IL-6 expression is impeded by antibody intervention in SARS-CoV-2 susceptible cell lines. *Sci. Rep.* **12**, 17047 (2022).
32. Lin, T. W. et al. Galectin-3 binding protein and galectin-1 interaction in breast cancer cell aggregation and metastasis. *J. Am. Chem. Soc.* **137**, 9685–9693 (2015).
33. Choi, Y. S. et al. Antibody-mediated blockade for galectin-3 binding protein in tumor secretome abrogates PDAC metastasis. *Proceedings of the National Academy of Sciences* 119, e2119048119 (2022).
34. Kim, Y. S. et al. Galectin-3 binding protein promotes cell motility in colon cancer by stimulating the shedding of protein tyrosine phosphatase kappa by proprotein convertase 5. *Biochem. Biophys. Res. Commun.* **404**, 96–102. https://doi.org/10.1016/j.bbrc.2010.11.071 (2011).
35. Loimaranta, V., Hepojoki, J., Laaksoaho, O. & Pulliainen, A. T. Galectin-3-binding protein: a multitask glycoprotein with innate immunity functions in viral and bacterial infections. *J. Leukoc. Biol.* **104**, 777–786 (2018).
36. Marchetti, A. et al. Expression of 90K (Mac-2 BP) correlates with distant metastasis and predicts survival in stage I non-small cell lung cancer patients. *Cancer Res.* **62**, 2535–2539 (2002).
37. Sun, L. et al. Functional screen for secreted proteins by monoclonal antibody library and identification of Mac-2 binding protein (Mac-2BP) as a potential therapeutic target and biomarker for lung cancer. *Mol. Cell. Proteom.* **12**, 395–406 (2013).
38. Tiedemann, K. et al. Exosomal release of L-Plastin by breast Cancer cells facilitates metastatic bone osteolysis. *Translational Oncol.* **12**, 462–474. https://doi.org/10.1016/j.tranon.2018.11.014 (2019).
39. Ciftci, E. et al. Comparative analysis of magnetically activated cell sorting and ultracentrifugation methods for exosome isolation. *Plos One.* **18**, e0282238 (2023).
40. Lyu, T. S. et al. The characterization of exosomes from fibrosarcoma cell and the useful usage of dynamic light scattering (DLS) for their evaluation. *PLoS One.* **16**, e0231994 (2021).
41. Taverna, S. et al. Amphiregulin contained in NSCLC-exosomes induces osteoclast differentiation through the activation of EGFR pathway. *Sci. Rep.* **7**, 3170. https://doi.org/10.1038/s41598-017-03460-y (2017).
42. Fan, J. T. et al. Exosomal lncRNA NEAT1 from cancer-associated fibroblasts facilitates endometrial cancer progression via miR-26a/b-5p-mediated STAT3/YKL-40 signaling pathway. *Neoplasia.* **23**, 692–703. https://doi.org/10.1016/j.neo.2021.05.004 (2021).
43. Kheradjoo, H., Nouralishahi, A., Hoseinzade Firozabadi, M. S. & Mohammadzadehsaliani, S. Mesenchymal stem/stromal (MSCs)-derived exosome inhibits retinoblastoma Y-79 cell line proliferation and induces their apoptosis. *Nanomed. Res. J.* **7**, 264–269 (2022).
44. Ghanta, P. et al. Efficacy assessment of methylcellulose-based thermoresponsive hydrogels loaded with gallium acetylacetonate in osteoclastic bone resorption. *Drug Deliv Transl Res.* **13**, 2533–2549. https://doi.org/10.1007/s13346-023-01336-5 (2023).
45. Hessel, E., Ghanta, P., Winschel, T., Melnyk, L. & Oyewumi, M. O. Fabrication of 3D-printed scaffolds loaded with gallium acetylacetonate for potential application in osteoclastic bone resorption. *Pharm. Dev. Technol.*, 1–39 (2024).
46. Zhou, Y. et al. Exosomes derived from pancreatic cancer cells induce osteoclast differentiation through the miR125a-5p/TNFRSF1B pathway. *OncoTargets Therapy*, 2727–2739 (2021).
47. Aghayev, M. et al. A high-fat diet increases hepatic mitochondrial turnover through restricted acetylation in a NAFLD mouse model. *Am. J. Physiology-Endocrinology Metabolism.* **325**, E83–E98. https://doi.org/10.1152/ajpendo.00310.2022 (2023).
48. Yu, L. et al. Exosomes derived from osteogenic tumor activate osteoclast differentiation and concurrently inhibit osteogenesis by transferring COL1A1-targeting miRNA-92a-1-5p. *J. Extracell. Vesicles.* **10**, e12056. https://doi.org/10.1002/jev2.12056 (2021).
49. Al-Rawashde, F. A. et al. Thymoquinone inhibits JAK/STAT and PI3K/Akt/ mTOR signaling pathways in MV4-11 and K562 myeloid leukemia cells. *Pharmaceuticals.* **15**, 1123 (2022).
50. Xu, L., Wu, Z., Zhou, Z., Yang, X. & Xiao, J. Intratibial injection of patient-derived tumor cells from giant cell tumor of bone elicits osteolytic reaction in nude mouse. *Oncol. Lett.* **16**, 4649–4655. https://doi.org/10.3892/ol.2018.9148 (2018).
51. Li, B. et al. A novel bioluminescence orthotopic mouse model for advanced lung cancer. *Radiat. Res.* **176**, 486–493. https://doi.org/10.1667/rr2565.1 (2011).
52. Puri, A. et al. Stealth oxime ether lipid vesicles promote delivery of functional DsiRNA in human lung cancer A549 tumor bearing mouse xenografts. *Nanomed. Nanotechnol. Biol. Med.* **44**, 102572. https://doi.org/10.1016/j.nano.2022.102572 (2022).

53. Dengler-Crish, C. M., Ball, H. C., Lin, L., Novak, K. M. & Cooper, L. N. Evidence of Wnt/β-catenin alterations in brain and bone of a tauopathy mouse model of Alzheimer's disease. *Neurobiol. Aging.* **67**, 148–158. https://doi.org/10.1016/j.neurobiolaging.2018.03.021 (2018).
54. Zhang, B. et al. Acetylation of KLF5 maintains EMT and tumorigenicity to cause chemoresistant bone metastasis in prostate cancer. *Nat. Commun.* **12**, 1714. https://doi.org/10.1038/s41467-021-21976-w (2021).
55. Wang, C. et al. Exosomes carrying ALDOA and ALDH3A1 from irradiated lung cancer cells enhance migration and invasion of recipients by accelerating glycolysis. *Mol. Cell. Biochem.* **469**, 77–87. https://doi.org/10.1007/s11010-020-03729-3 (2020).
56. Chiou, W. F., Huang, Y. L. & Liu, Y. W. +)-Vitisin A inhibits osteoclast differentiation by preventing TRAF6 ubiquitination and TRAF6-TAK1 formation to suppress NFATc1 activation. *PLoS One.* **9**, e89159 (2014).
57. Chen, K. et al. Shikonin mitigates ovariectomy-induced bone loss and RANKL-induced osteoclastogenesis via TRAF6-mediated signaling pathways. *Biomed. Pharmacother.* **126**, 110067 (2020).
58. Zhang, J. et al. Loureirin B downregulates osteoclast differentiation of bone marrow macrophages by targeting the MAPK signaling pathway. *Sci. Rep.* **12**, 14382. https://doi.org/10.1038/s41598-022-18287-5 (2022).
59. Shen, X. et al. Demethoxycucumin protects MDA-MB-231 cells induced bone destruction through JNK and ERK pathways inhibition. *Cancer Chemother. Pharmacol.* **87**, 487–499. https://doi.org/10.1007/s00280-020-04198-7 (2021).
60. Rathod, B. et al. Tartrate-resistant acid phosphatase (TRAP/ACP5) promotes bone length, regulates cortical and trabecular bone mass, and maintenance growth plate architecture and width in a sex-and site-specific manner in mice. *Bone*, **117223** (2024).
61. Hu, J. et al. The protective effect of WKYMVm peptide on inflammatory osteolysis through regulating NF-κB and CD9/gp130/STAT3 signalling pathway. *J. Cell. Mol. Med.* **24**, 1893–1905 (2020).
62. Zheng, X. Q. et al. Incidence, prognostic factors, and a nomogram of lung cancer with bone metastasis at initial diagnosis: a population-based study. *Transl Lung Cancer Res.* **8**, 367–379. https://doi.org/10.21037/tlcr.2019.08.16 (2019).
63. Kimura, T. Multidisciplinary approach for bone metastasis: a review. *Cancers.* **10**, 156 (2018).
64. Oh, I. R., Raymundo, B., Kim, M. & Kim, C. W. Mesenchymal stem cells co-cultured with colorectal cancer cells showed increased invasive and proliferative abilities due to its altered p53/TGF-β1 levels. *Biosci. Biotechnol. Biochem.* **84**, 256–267. https://doi.org/10.1080/09168451.2019.1676692 (2020).
65. Hasan, H. et al. Extracellular vesicles released by non-small cell lung cancer cells drive invasion and permeability in non-tumorigenic lung epithelial cells. *Sci. Rep.* **12**, 972. https://doi.org/10.1038/s41598-022-04940-6 (2022).
66. Hulley, P. A. & Knowles, H. J. A New Method to Sort differentiating osteoclasts into defined homogeneous subgroups. *Cells.* **11**, 3973 (2022).
67. Wang, M. et al. Thrombospondin enhances RANKL-dependent osteoclastogenesis and facilitates lung cancer bone metastasis. *Biochem. Pharmacol.* **166**, 23–32. https://doi.org/10.1016/j.bcp.2019.05.005 (2019).
68. Søe, K. Osteoclast Fusion: physiological regulation of multinucleation through heterogeneity—potential implications for drug sensitivity. *Int. J. Mol. Sci.* **21**, 7717 (2020).
69. Zou, B. et al. Oridonin ameliorates inflammation-induced bone loss in mice via suppressing DC-STAMP expression. *Acta Pharmacol. Sin.* **42**, 744–754. https://doi.org/10.1038/s41401-020-0477-4 (2021).
70. Chen, Y. et al. Dendritic cells-derived interferon-λ1 ameliorated inflammatory bone destruction through inhibiting osteoclastogenesis. *Cell Death Dis.* **11**, 414. https://doi.org/10.1038/s41419-020-2612-z (2020).
71. Chiu, Y. H. et al. Regulation of human osteoclast development by dendritic cell-specific transmembrane protein (DC-STAMP). *J. Bone Miner. Res.* **27**, 79–92. https://doi.org/10.1002/jbmr.531 (2012).
72. Isaac, R., Reis, F. C. G., Ying, W. & Olefsky, J. M. Exosomes as mediators of intercellular crosstalk in metabolism. *Cell Metabol.* **33**, 1744–1762 (2021).
73. Solimani, F. et al. Characterizing the proteome of bullous pemphigoid blister fluid utilizing tandem mass tag labeling coupled with LC–MS/MS. *Arch. Dermatol. Res.* **314**, 921–928 (2022).
74. Capone, E. et al. Targeting vesicular LGALS3BP by an antibody-drug conjugate as novel therapeutic strategy for neuroblastoma. *Cancers.* **12**, 2989 (2020).
75. Song, Y. et al. Plasma exosomes from endometrial cancer patients contain LGALS3BP to promote endometrial cancer progression. *Oncogene.* **40**, 633–646. https://doi.org/10.1038/s41388-020-01555-x (2021).
76. Woo, J. K. et al. Lectin, galactoside-binding soluble 3 binding protein promotes 17-N-Allylamino-17-demethoxygeldanamycin resistance through PI3K/Akt pathway in lung cancer cell line. *Mol. Cancer Ther.* **16**, 1355–1365 (2017).
77. Dufrusine, B. et al. Extracellular LGALS3BP: a potential disease marker and actionable target for antibody-drug conjugate therapy in glioblastoma. *Mol. Oncol.* **17**, 1460–1473. https://doi.org/10.1002/1878-0261.13453 (2023).
78. Nielsen, M. et al. Increased synovial galectin-3 induce inflammatory fibroblast activation and osteoclastogenesis in patients with rheumatoid arthritis. *Scand. J. Rheumatol.* **52**, 33–41 (2023).
79. Li, C. H. et al. Galectins in cancer and the microenvironment: functional roles, therapeutic developments, and perspectives. *Biomedicines.* **9**, 1159 (2021).

Acknowledgements

Author contributions

Material preparation, data collection and analysis with respect to cell and animal studies were performed by PG, EH and MO. Proteomic studies were carried out by PG, AA, MA, SI and TK. PG wrote the manuscript and other authors contributed to data presentation and editing. MO was also responsible for conceptualization of the research question, project supervision, administration, funding acquisition, experiment validation, manuscript review and editing. All authors read and approved the final manuscript.

Declarations

Competing interests

The authors declare no competing interests.

Additional information

Supplementary Information The online version contains supplementary material available at https://doi.org/10.1038/s41598-024-79006-w.

Correspondence and requests for materials should be addressed to M.O.O.

Reprints and permissions information is available at www.nature.com/reprints.

Publisher's note Springer Nature remains neutral with regard to jurisdictional claims in published maps and institutional affiliations.